Ranging Sensor Fusion in LISA Data Processing: Treatment of Ambiguities, Noise, and On-Board Delays in LISA Ranging Observables

Jan Niklas Reinhardt,[1,2,*] Martin Staab,[1,2] Kohei Yamamoto,[1,2] Jean-Baptiste Bayle,[3] Aurélien Hees,[4] Olaf Hartwig,[4] Karsten Wiesner,[1,2] and Gerhard Heinzel[1,2]

[1] *Max-Planck-Institut für Gravitationsphysik (Albert-Einstein-Institut), Callinstraße 38, 30167 Hannover, Germany*
[2] *Leibniz Universität Hannover, Welfengarten 1, 30167 Hannover, Germany*
[3] *University of Glasgow, Glasgow G12 8QQ, United Kingdom*
[4] *SYRTE, Observatoire de Paris, Université PSL, CNRS, Sorbonne Université, LNE, 61 avenue de l'observatoire 75014 Paris, France*

Interspacecraft ranging is crucial for the suppression of laser frequency noise via time-delay interferometry (TDI). So far, the effect of on-board delays and ambiguities in the LISA ranging observables was neglected in LISA modelling and data processing investigations. In reality, on-board delays cause offsets and timestamping delays in the LISA measurements, and PRN ranging is ambiguous, as it only determines the range up to an integer multiple of the pseudo-random noise (PRN) code length. In this article, we identify the four LISA ranging observables: PRN ranging, the sideband beatnotes at the interspacecraft interferometer, TDI ranging, and ground-based observations. We derive their observation equations in the presence of on-board delays, noise, and ambiguities. We then propose a three-stage ranging sensor fusion to combine these observables in order to gain optimal ranging estimates. We propose to calibrate the on-board delays on ground and to compensate the associated offsets and timestamping delays in an initial data treatment (stage 1). We identify the ranging-related routines, which need to run continuously during operation (stage 2), and implement them numerically. Essentially, this involves the reduction of ranging noise, for which we develop a Kalman filter combining the PRN ranging and the sideband beatnotes. We further implement crosschecks for the PRN ranging ambiguities and offsets (stage 3). We show that both ground-based observations and TDI ranging can be used to resolve the PRN ranging ambiguities. Moreover, we apply TDI ranging to estimate the PRN ranging offsets.

I. INTRODUCTION

The Laser Interferometer Space Antenna (LISA), due for launch in 2034, is an ESA-led mission for space-based gravitational-wave detection in the frequency band between 0.1 mHz and 1 Hz [1]. LISA consists of three satellites forming an approximate equilateral triangle with an armlength of 2.5 Gm, in a heliocentric orbit that trails or leads Earth by about 20 degrees. Six infrared laser links with a nominal wavelength of 1064 nm connect the three spacecraft (SC), whose relative motion necessitates the usage of heterodyne interferometry. Phasemeters are used to extract the phases of the corresponding beatnotes [2], in which gravitational-waves manifest in form of microcycle deviations equivalent to picometer variations in the interspacecraft ranges.

The phasemeter output, however, is obscured by various instrumental noise sources. They must be suppressed to fit in the LISA noise budget of $10\,\mathrm{pm\,Hz^{-0.5}}$ (single link) [3], otherwise they would bury the gravitational-wave signals. Dedicated data processing algorithms are being developed for each of these instrumental noise sources, their subsequent execution is referred to as initial noise reduction pipeline (INReP). The dominating noise source in LISA is by far the laser frequency noise due to the armlength differences in the order of 1% (25 000 km). It must be reduced by more than 8 orders of magnitude. This is achieved by time-delay interferometry (TDI), which combines the various beatnotes with the correct delays to virtually form equal-optical-path-length interferometers, in which laser frequency noise naturally cancels [4, 5]. The exact definition of these delays depends on the location of TDI within the INReP (see fig. 1) [6], but wherever we place it, some kind of information about the absolute interspacecraft ranges is required.

Yet, absolute ranges are not a natural signal in a continuous-wave heterodyne laser interferometer such as LISA. Therefore, a ranging scheme based on pseudo-random noise (PRN) codes is implemented [7–9]. Each SC houses a free-running ultra-stable oscillator (USO) as timing reference. It defines the spacecraft elapsed time (SCET). PRN codes generated according to the respective SCETs are imprinted onto the laser beams by phase-modulating the carrier. The comparison of a PRN code received from a distant SC, hence generated according to the distant SCET, with a local copy enables a measurement of the pseudorange: the pseudorange is commonly defined as the difference between the SCET of the receiving SC at the event of reception and the SCET of the emitting SC at the event of emission [10]. It represents a combination of the true geometrical range (light travel time) with the offset between the two involved SCETs (see eq. A5).

In the baseline TDI topology (upper row in fig. 1), TDI is performed after SCET synchronization to the barycen-

* janniklas.reinhardt@aei.mpg.de

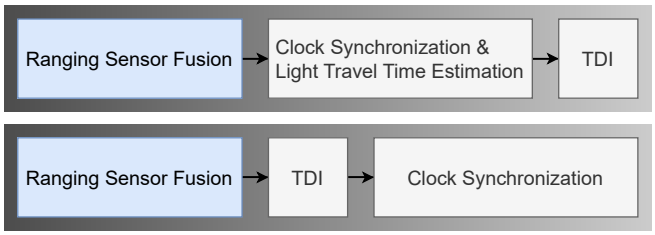

Figure 1. In the baseline TDI topology (upper part) we perform TDI after clock synchronization to TCB, the delays are given by the light travel times. In the alternative TDI topology (lower part) we execute TDI without clock synchronization and apply the pseudoranges as delays [6]. Both topologies rely on a ranging sensor fusion.

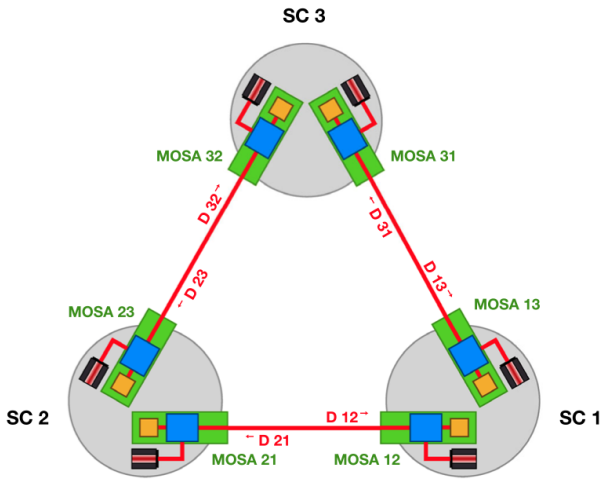

Figure 2. LISA labeling conventions (from [14]). The SC are labeled clockwise. The MOSAs are labeled by 2 indices: the first one indicates the SC they are located at, the second one the SC they are oriented to. The measurements and related quantities (optical links, pseudoranges, etc.) share the indices of the MOSAs they are measured at. Below, we distinguish between left-handed MOSAs (12, 23, 31) and right-handed MOSAs (13, 32, 21).

tric coordinate time (TCB), the light travel times are used as delays. The pseudoranges comprise information about both the light travel times and the SCET offsets required for synchronizing the clocks (see appendix A). A Kalman filter can be used to disentangle the pseudoranges in order to retrieve light travel times and SCET offsets [11]. In the alternative TDI topology (lower row in fig. 1), the pseudoranges are directly used as delays. In that topology, TDI is executed on the unsynchronized beatnotes sampled according to the respective SCETs [6].

However, PRN ranging (PRNR) does not directly provide the pseudoranges but requires three treatments. First, due to the finite PRN code length (we assume 400 km), PRNR measures the pseudoranges modulo an ambiguity [7]. Secondly, PRNR is limited by white ranging noise with an RMS amplitude of about 1 m when sampled at 4 Hz [9]. Thirdly, on-board delays due to signal propagation and processing cause offsets and timestamping delays in the PRNR. There are three additional pseudorange observables to resolve these difficulties: ground-based observations provide inaccurate but unambiguous pseudorange estimates; time-delay interferometric ranging (TDIR) turns TDI upside-down seeking a model for the delays that minimizes the laser frequency noise in the TDI combinations [12]; the sideband beatnotes include information about the time derivatives of the pseudoranges [6]. The combination of these four pseudorange observables in order to form optimal pseudorange estimates is referred to as *ranging sensor fusion* in the course of this article. It is common to both TDI topologies (see fig. 1) and consequently a crucial stage of the INReP.

In section II, we first specify the pseudorange definition. We then derive the observation equations of the four pseudorange observables carefully considering the effects of the on-board delays. In section III, we introduce a three-stage ranging sensor fusion consisting of an initial data treatment, a core ranging processing, and crosschecks. In the initial data treatment, we propose to compensate for the offsets and timestamping delays caused by the on-board delays. We identify PRNR unwrapping and noise reduction as the ranging processing steps that need to run continuously during operation. In parallel to this core ranging processing, we propose crosschecks of the PRNR ambiguities and offsets. We implement the core ranging processing and the crosschecks numerically. In section IV we discuss the performance of this implementation, and conclude in section V.

II. RANGING MEASUREMENTS

Each SC houses an ultra-stable oscillator (USO) generating an 80 MHz clock signal, the phasemeter clock (PMC). The PMC can be considered as the timing reference on board the SC (see fig. 3), its associated counter is referred to as spacecraft elapsed time (SCET):

$$\mathrm{SCET}(n) = \sum_{1}^{n} \frac{1}{80\,\mathrm{MHz}}. \tag{1}$$

The SCET, denoted by $\hat{\tau}_i$, differs from the barycentric coordinate time (TCB), denoted by t, due to instrumental clock drifts and jitters, and due to relativistic effects. Following the notation of [13], we use superscripts to indicate a quantity to be expressed as function of a certain time scale, e.g., $\hat{\tau}_1^t$ denotes the SCET of SC 1 as function of TCB. Note that

$$\hat{\tau}_i^{\hat{\tau}_i}(\tau) = \tau. \tag{2}$$

Each SC contains two movable optical sub-assemblies (MOSAs) connected by an optical fibre (see fig. 2 for

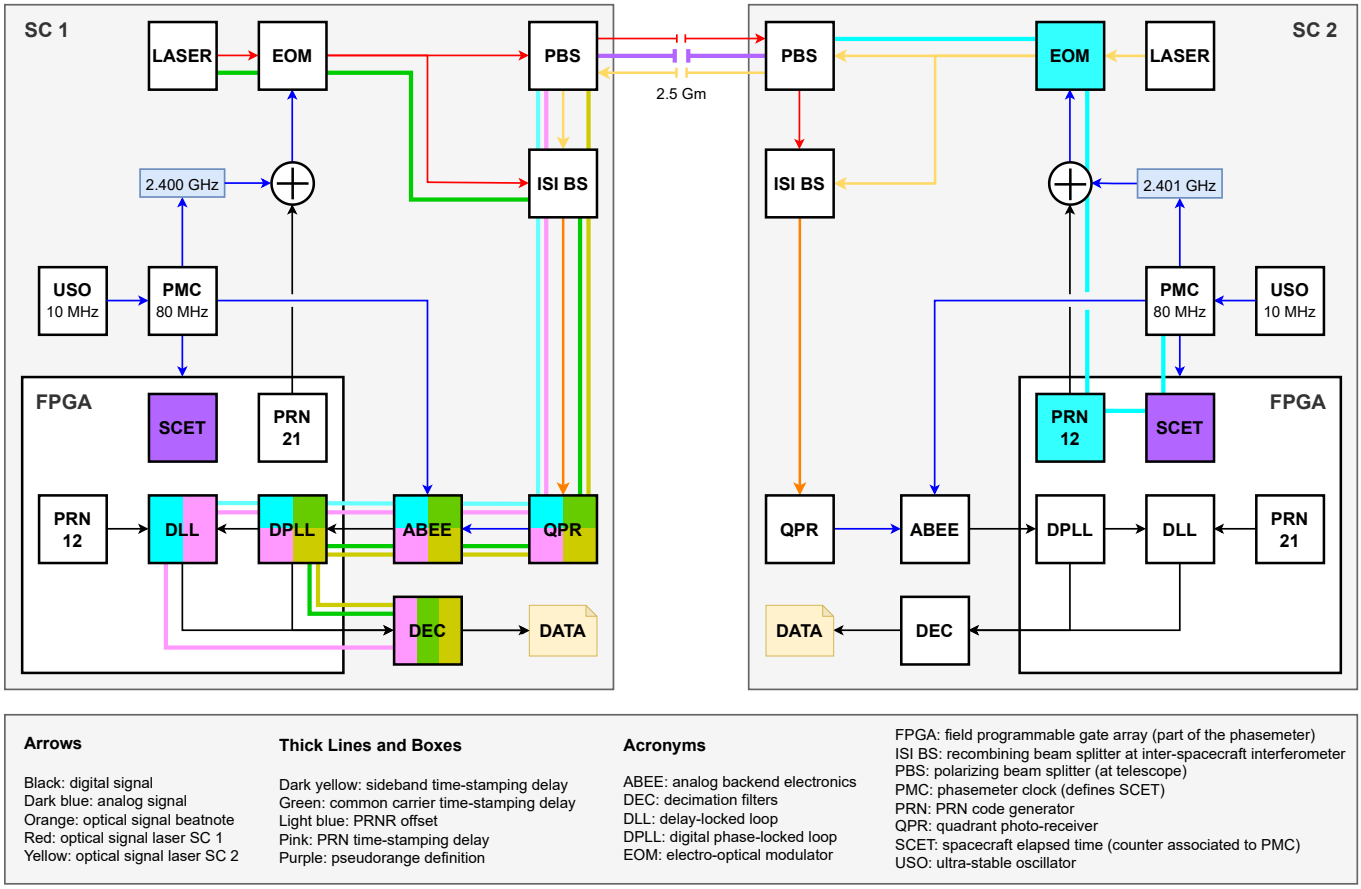

Figure 3. We trace a local laser (red arrows) and a distant laser (yellow arrows) to the ISI BSs on both SC, where they interfere and form beatnotes (orange arrows). Before, the carriers are phase-modulated with the GHz clock and the PRN signals (follow the arrows from the PMC and the PRN to the EOM). We show the USO frequency distribution (follow the blue arrows after the USOs) and illustrate the on board signal processing (follow the arrows after the QPRs). Constituents of the pseudorange are marked purple. These are the light travel time between the PBSs (at the telescopes) and the transformation between the two SCETs (considered at the PBS of the receiving SC). In light blue, we mark the PRN ranging offset from the pseudorange. We identify the common carrier, sideband, and PRN timestamping delays in green, dark yellow, and pink, respectively.

the labeling conventions). Each MOSA has an associated laser and houses a telescope, a free-falling test mass marking the end of the corresponding optical link, and an optical bench with three interferometers: the interspacecraft interferometer (ISI), in which the gravitational-wave signals eventually appear, the reference interferometer (RFI) to compare local and adjacent lasers, and the test-mass interferometer (TMI) to sense the optical bench motion with respect to the free-falling test mass in direction of the optical link. The MHz beatnotes in these interferometers are detected with quadrant-photoreceivers (QPRs). They are digitized in analog-to-digital converters (ADCs) driven by the PMCs. Phasemeters extract the beatnote phases[1] using digital phase-locked loops (DPLLs), which are then downsampled to 4 Hz in a multi-stage decimation procedure (DEC) and telemetered to Earth.

A. The pseudorange and on-board delays

The pseudorange, denoted by $R_{ij}^{\hat{\tau}_i}$, is commonly defined as the difference between the SCET of the receiving SC at the event of reception and the SCET of the emitting SC at the event of emission [10]. It represents a combination of the light travel time between the emission at SC j and the reception at SC i, and the differential SCET offset (see eq. A5). However, considering the complexity of the LISA metrology system, this definition appears to be rather vague: to what exactly do we relate the events of emission and reception? Two specifications are required here: we need to locate emission and reception, and we need to define the actual events. It is convenient to con-

[1] In the current design, the phasemeters deliver the beatnote frequencies with occasional phase anchor points.

sider emission and reception at the respective polarizing beam splitters (PBSs) in front of the telescopes (denoted PBS1 in [15]), and to treat the on-board signal propagation and processing on both SC as on-board delays. Thus, we clearly separate the pseudorange from on-board delays. This definition is not unique, the events of emission and reception could be located elsewhere, assuming that the on-board delays are defined accordingly. The LISA optical links do not involve delta-pulse-like events. In order to define the actual events of emission and reception we, instead, use the instants when the light phase changes at the beginning of the first PRN code chip. At first glance, the PRN code might seem unfavorable for the pseudorange definition, as PRN and carrier phase are oppositely affected by the solar wind: the PRN phase is delayed by the group-delay, while the carrier phase is advanced by the phase delay. However, these effects are at the order of 10 pm (see appendix C), whereas our best pseudorange estimates are at 0.1 mm accuracy. Consequently, the solar wind dispersion can be neglected in the pseudorange definition.

When expressing the interferometric measurements according to this specified pseudorange definition, we need to consider the excluded on-board signal propagation and processing. For that purpose, we introduce two kinds of delay operators by their action on a function $f^{\hat{\tau}_j}$. The on-board delay operator describes delays due to on-board signal propagation and processing and is defined on the same SCET as the function it is acting on:

$$\mathbf{D}_x^{\hat{\tau}_j}\, f^{\hat{\tau}_j}(\tau) = f^{\hat{\tau}_j}\left(\tau - d_x^{\hat{\tau}_j}(\tau)\right). \tag{3}$$

x is a place holder for any on-board delay, e.g., $\mathbf{D}_{\mathrm{pbs}\,\leftarrow\,\mathrm{l}}$ denotes the optical path length from the laser to the PBS and $\mathbf{D}_{\mathrm{dec}}$ the decimation filter group delay. The interspacecraft delay operator is defined on a different SCET than the function it is acting on and applies the pseudorange as delay:

$$\mathbf{D}_{ij}^{\hat{\tau}_i}\, f^{\hat{\tau}_j}(\tau) = f^{\hat{\tau}_j}\left(\tau - R_{ij}^{\hat{\tau}_i}(\tau)\right). \tag{4}$$

For on-board delays that differ between carrier, PRN, and sideband signals, we add the superscripts *car*, *prn*, and *sb*, respectively. To trace the full path of a signal from the distant SC, we need to combine the interspacecraft delay operator for the interspacecraft signal propagation and the SCET conversion (considered at the PBS of the receiving SC) with on-board delay operators on both SC. The application of a delay operator to another time-dependent delay operator results in nested delays:

$$\mathbf{D}_x^{\hat{\tau}_i}\,\mathbf{D}_{ij}^{\hat{\tau}_i} f^{\hat{\tau}_j}(\tau) = f^{\hat{\tau}_j}\left(\tau - d_x^{\hat{\tau}_i}(\tau) - R_{ij}^{\hat{\tau}_i}\left(\tau - d_x^{\hat{\tau}_i}(\tau)\right)\right). \tag{5}$$

For a constant delay operator $\mathbf{D}_x$ we can define the associated advancement operator $\mathbf{A}_x$ acting as its inverse:

$$\mathbf{A}_x^{\hat{\tau}_j}\, f^{\hat{\tau}_j}(\tau) = f^{\hat{\tau}_j}\left(\tau + d_x^{\hat{\tau}_j}\right), \tag{6}$$

$$\mathbf{A}_x\,\mathbf{D}_x\, f^{\hat{\tau}_j}(\tau) = f^{\hat{\tau}_j}\left(\tau - d_x^{\hat{\tau}_j} + d_x^{\hat{\tau}_j}\right) = f^{\hat{\tau}_j}(\tau). \tag{7}$$

For advancement operators associated to propagation delays, e.g., the optical path length from the laser to the PBS, we write

$$\mathbf{D}^{-1}_{\mathrm{pbs}\,\leftarrow\,\mathrm{l}} = \mathbf{A}_{\mathrm{l}\,\leftarrow\,\mathrm{pbs}}, \tag{8}$$

the subscript underlines that the advancement operator undoes the signal propagation. Below, we consider on-board delays as constant or slowly time varying so that their associated advancement operators are well-defined.

What does the specified pseudorange definition imply for TDI in the context of on-board delays? In [6] the pseudoranges are said to be the delays that are to be applied in TDI in the alternative topology. To find out whether this statement holds, we write down the ISI carrier beatnotes in the presence of on-board delays using the above defined delay operators:

$$\mathrm{ISI}_{ij}^{\hat{\tau}_i}(\tau) = \mathbf{D}^{\mathrm{car},\,\hat{\tau}_i}_{\mathrm{dec}\,\leftarrow\,\mathrm{bs}}\Big(\mathbf{D}^{\hat{\tau}_i}_{\mathrm{bs}\,\leftarrow\,\mathrm{pbs}}\,\mathbf{D}^{\hat{\tau}_i}_{ij}\,\mathbf{D}^{\hat{\tau}_j}_{\mathrm{pbs}\,\leftarrow\,\mathrm{l}}\Phi^{\hat{\tau}_j}_{ji}(\tau) - \mathbf{D}^{\hat{\tau}_i}_{\mathrm{bs}\,\leftarrow\,\mathrm{l}}\,\Phi^{\hat{\tau}_i}_{ij}(\tau)\Big). \tag{9}$$

$\mathbf{D}_{\mathrm{pbs}\,\leftarrow\,\mathrm{l}}$ denotes the optical path length from the laser to the PBS (before transmission), $\mathbf{D}_{\mathrm{bs}\,\leftarrow\,\mathrm{pbs}}$ is the optical path length from the PBS to the recombining beam splitter of the interspacecraft interferometer (ISI BS) (after reception), and $\mathbf{D}_{\mathrm{bs}\,\leftarrow\,\mathrm{l}}$ denotes the optical path length from the local laser to the ISI BS. These optical path lengths are in the order of 10 cm to 1 m [15]. $\mathbf{D}^{\mathrm{car}}_{\mathrm{dec}\,\leftarrow\,\mathrm{bs}}$ denotes the delay from the ISI BS to the decimation filters, it differs for sideband and PRN signals. The dominating part of $\mathbf{D}^{\mathrm{car}}_{\mathrm{dec}\,\leftarrow\,\mathrm{bs}}$ is the group delay of the decimation filters in the order of 1 s. To identify the delay we need to apply in TDI, it is convenient to split the delays in eq. 9 into a common and an uncommon delay by inserting $\mathbf{D}^{\hat{\tau}_i}_{\mathrm{bs}\,\leftarrow\,\mathrm{l}}\,\mathbf{A}^{\hat{\tau}_i}_{\mathrm{l}\,\leftarrow\,\mathrm{bs}} = \mathbf{1}$ in front of the bracket:

$$\mathrm{ISI}_{ij}^{\hat{\tau}_i}(\tau) = \mathbf{C}_i^{\mathrm{car},\,\hat{\tau}_i}\left(\mathbf{U}_{ij}^{\hat{\tau}_i}\,\Phi_{ji}^{\hat{\tau}_j}(\tau) - \Phi_{ij}^{\hat{\tau}_i}(\tau)\right), \tag{10}$$

$$\mathbf{C}_i^{\mathrm{car},\,\hat{\tau}_i} = \mathbf{D}^{\mathrm{car},\,\hat{\tau}_i}_{\mathrm{dec}\,\leftarrow\,\mathrm{bs}}\,\mathbf{D}^{\hat{\tau}_i}_{\mathrm{bs}\,\leftarrow\,\mathrm{l}}, \tag{11}$$

$$\mathbf{U}_{ij}^{\hat{\tau}_i} = \mathbf{A}^{\hat{\tau}_i}_{\mathrm{l}\,\leftarrow\,\mathrm{bs}}\,\mathbf{D}^{\hat{\tau}_i}_{\mathrm{bs}\,\leftarrow\,\mathrm{pbs}}\,\mathbf{D}^{\hat{\tau}_i}_{ij}\,\mathbf{D}^{\hat{\tau}_j}_{\mathrm{pbs}\,\leftarrow\,\mathrm{l}}. \tag{12}$$

$\mathbf{C}_i^{\mathrm{car}}$ denotes the common delay of the local and the distant carrier phase. $\mathbf{U}_{ij}$ is the uncommon delay that only applies to the distant carrier phase. We refer to $\mathbf{C}_i^{\mathrm{car}}$ and $\mathbf{U}_{ij}$ as common and uncommon carrier delay, respectively. To see how these delays affect the carrier beatnotes, we expand eq. 10:

$$\mathrm{ISI}_{ij}^{\hat{\tau}_i}(\tau) = \Phi_{ji}^{\hat{\tau}_j}\left(\tau - c_i^{\hat{\tau}_i} - u_{ij}^{\hat{\tau}_i}\left(\tau - c_i^{\hat{\tau}_i}\right)\right) - \Phi_{ij}^{\hat{\tau}_i}\left(\tau - c_i^{\hat{\tau}_i}\right). \tag{13}$$

The common carrier delay causes a timestamping delay in both the laser phases and the uncommon carrier delay (essentially the pseudorange). It can be compensated by

application of its associated advancement operator:

$$\left(\mathbf{C}_i^{\mathrm{car},\,\hat{\tau}_i}\right)^{-1}\mathrm{ISI}_{ij}^{\hat{\tau}_i}(\tau)=\mathbf{U}_{ij}^{\hat{\tau}_i}\,\Phi_{ji}^{\hat{\tau}_j}(\tau)-\Phi_{ij}^{\hat{\tau}_i}(\tau), \tag{14}$$

$$\begin{aligned}\left(\mathbf{C}_i^{\mathrm{car},\,\hat{\tau}_i}\right)^{-1}&=\left(\mathbf{D}_{\mathrm{bs}\,\leftarrow\,\mathrm{l}}^{\hat{\tau}_i}\right)^{-1}\left(\mathbf{D}_{\mathrm{dec}\,\leftarrow\,\mathrm{bs}}^{\mathrm{car},\,\hat{\tau}_i}\right)^{-1}\\&=:\mathbf{A}_{\mathrm{l}\,\leftarrow\,\mathrm{dec}}^{\mathrm{car},\,\hat{\tau}_i}.\end{aligned} \tag{15}$$

TDI is blind to the common carrier delay, as it equally delays the laser phases and the pseudorange. Hence, from the perspective of TDI eq. 9 and eq. 14 are equivalent. Nevertheless, the compensation of the common carrier delay is important for the synchronization of the measurements to TCB. We propose to calibrate $\mathbf{C}_i^{\mathrm{car}}$ on ground, so that during operation it can be compensated in an initial data treatment by application of its associated advancement operator (see eq. 14). After this initial data treatment, the uncommon carrier delay constitutes the delay that is to be applied in TDI in the alternative topology. It is composed of the optical path length delay from the distant laser source to the local ISI BS and the optical path length advancement from the ISI BS to the local laser source. Hence, it can be thought of as the differential optical path length from both lasers to the ISI BS. To construct the uncommon carrier delay, we need to measure the optical path lengths laser to PBS, PBS to ISI BS, and laser to ISI BS on ground, and we need to measure the pseudorange during operation. The sections II B to II E cover the four pseudorange observables. Before, we close this section with a few comments on the common carrier delay.

Parts of the common carrier delay are slowly time varying. To analyze the origin of this time dependence we decompose $\mathbf{C}_i^{\mathrm{car}}$ into

$$\begin{aligned}\mathbf{C}_i^{\mathrm{car}}=&\,\mathbf{D}_{\mathrm{dec}}^{\mathrm{car}}\,\mathbf{D}_{\mathrm{dpll}}^{\mathrm{car}}\,\mathbf{D}_{\mathrm{dpll}\,\leftarrow\,\mathrm{abee}}\,\mathbf{D}_{\mathrm{abee}}^{\mathrm{car}}\\&\mathbf{D}_{\mathrm{abee}\,\leftarrow\,\mathrm{qpr}}\,\mathbf{D}_{\mathrm{qpr}}^{\mathrm{car}}\,\mathbf{D}_{\mathrm{qpr}\,\leftarrow\,\mathrm{bs}}\,\mathbf{D}_{\mathrm{bs}\,\leftarrow\,\mathrm{l}},\end{aligned} \tag{16}$$

these constituents are marked green in fig. 3. The dominating contribution is by far the decimation filter group delay $\mathbf{D}_{\mathrm{dec}}^{\mathrm{car}}$ in the order of 1 s. It is constant and predetermined by the design of the decimation filters. The group delays of the quadrant-photo-receiver $\mathbf{D}_{\mathrm{qpr}}^{\mathrm{car}}$ and the analog backend electronics[2] $\mathbf{D}_{\mathrm{abee}}^{\mathrm{car}}$ depend amongst others on the beatnote frequency [16]. Hence, they change over time and differ between carrier, sideband, and PRN signals. Together with the cable delays $\mathbf{D}_{\mathrm{abee}\leftarrow\,\mathrm{qpr}}$ and $\mathbf{D}_{\mathrm{dpll}\leftarrow\,\mathrm{abee}}$ they can amount to 10 m. The DPLL delay $\mathbf{D}_{\mathrm{dpll}}^{\mathrm{car}}$ depends on the time-dependent beatnote amplitude. The higher this amplitude the smaller $\mathbf{D}_{\mathrm{dpll}}^{\mathrm{car}}$ [2, 17]. $\mathbf{D}_{\mathrm{qpr}\,\leftarrow\,\mathrm{bs}}$ and $\mathbf{D}_{\mathrm{bs}\,\leftarrow\,\mathrm{l}}$, for completeness, denote the optical path lengths from the local laser to the QPR in the order of 10 cm to 1 m [15]. We propose to individually calibrate all constituents of $\mathbf{C}_i^{\mathrm{car}}$ on ground. The time-dependent ones should be calibrated for all combinations of the time-dependent parameters. Hence, during operation they can be constructed with the help of the SC monitors, which provide the corresponding parameter values, e.g., beatnote frequency and amplitude.

[2] The analog backend electronics comprise analog signal amplifiers, analog low-pass filters, and the ADC.

B. PRN ranging (PRNR)

A set of 6 pseudo-random noise (PRN) sequences has been computed such that the cross-correlations and the auto-correlations for nonzero delays are minimized. These PRN codes are associated to the 6 optical links in the LISA constellation. The PRN codes are generated according to the respective PMCs and imprinted onto the laser beams by phase-modulating the carriers in electro-optical modulators (EOMs). In each phasemeter, DPLLs are applied to extract the beatnote phases. The PRN codes show up in the DPLL error signals since the DPLL bandwidth of 10 kHz to 100 kHz is lower than the PRN chipping rate of about 1 MHz. In a delay-locked loop (DLL), these error signals are correlated with PRN codes generated according to the local SCET. This correlation yields a pseudorange measurement, we refer to it as PRN ranging (PRNR) [7, 8].

We now derive the PRNR observation equation carefully taking into account on-board delays. We model the path of the PRN code from the distant SC to the local DLL by applying delay operators to the distant SCET:

$$\mathbf{D}_{\mathrm{dll}\,\leftarrow\,\mathrm{pbs}}^{\mathrm{prn},\,\hat{\tau}_i}\,\mathbf{D}_{ij}^{\hat{\tau}_i}\,\mathbf{D}_{\mathrm{pbs}\,\leftarrow\,\mathrm{pmc}}^{\mathrm{prn},\,\hat{\tau}_j}\,\hat{\tau}_j^{\hat{\tau}_j}(\tau). \tag{17}$$

The two on-board delays can be decomposed into

$$\begin{aligned}\mathbf{D}_{\mathrm{pbs}\,\leftarrow\,\mathrm{pmc}}^{\mathrm{prn}}=&\,\mathbf{D}_{\mathrm{pbs}\,\leftarrow\,\mathrm{eom}}\,\mathbf{D}_{\mathrm{eom}\,\leftarrow\,\mathrm{prn}}\\&\mathbf{D}_{\mathrm{prn}}\,\mathbf{D}_{\mathrm{prn}\,\leftarrow\,\mathrm{pmc}},\end{aligned} \tag{18}$$

$$\begin{aligned}\mathbf{D}_{\mathrm{dll}\,\leftarrow\,\mathrm{pbs}}^{\mathrm{prn}}=&\,\mathbf{D}_{\mathrm{dll}}\,\mathbf{D}_{\mathrm{dpll}}^{\mathrm{prn}}\,\mathbf{D}_{\mathrm{dpll}\,\leftarrow\,\mathrm{abee}}\,\mathbf{D}_{\mathrm{abee}}^{\mathrm{prn}}\,\mathbf{D}_{\mathrm{abee}\,\leftarrow\,\mathrm{qpr}}\\&\mathbf{D}_{\mathrm{qpr}}^{\mathrm{prn}}\,\mathbf{D}_{\mathrm{qpr}\,\leftarrow\,\mathrm{bs}}\,\mathbf{D}_{\mathrm{bs}\,\leftarrow\,\mathrm{pbs}}.\end{aligned} \tag{19}$$

$\mathbf{D}_{\mathrm{pbs}\,\leftarrow\,\mathrm{pmc}}^{\mathrm{prn}}$ consists of the cable delays from the PMC to the EOM, the processing delay due to the PRN code generation, and the optical path length from the EOM to the PBS. All these delays are constant at the sensitive scale of PRNR, so that we do not have to consider delay nesting in $\mathbf{D}_{\mathrm{pbs}\,\leftarrow\,\mathrm{pmc}}^{\mathrm{prn}}$. We added the superscript *prn* because this path is different for the sideband signal. $\mathbf{D}_{\mathrm{dll}\,\leftarrow\,\mathrm{pbs}}^{\mathrm{prn}}$ is explained in the next paragraph as part of the PRN timestamping delay. At the DLL, the received PRN codes are correlated with identical codes generated according to the local SCET. We model this correlation as the difference between the local SCET and the delayed distant SCET (eq. 17), and we apply $\mathbf{D}_{\mathrm{dec}}^{\mathrm{prn}}$ to model the group delay of the decimation filters applicable to PRN ranging:

$$\mathbf{D}_{\mathrm{dec}}^{\mathrm{prn}}\left(\hat{\tau}_i^{\hat{\tau}_i}(\tau)-\mathbf{D}_{\mathrm{dll}\,\leftarrow\,\mathrm{pbs}}^{\mathrm{prn},\,\hat{\tau}_i}\,\mathbf{D}_{ij}^{\hat{\tau}_i}\,\mathbf{D}_{\mathrm{pbs}\,\leftarrow\,\mathrm{pmc}}^{\mathrm{prn},\,\hat{\tau}_j}\,\hat{\tau}_j^{\hat{\tau}_j}(\tau)\right). \tag{20}$$

To see how the on-board delays affect the PRNR we expand eq. 20 applying eq. 2:

$$\begin{aligned}\mathbf{D}^{\mathrm{prn}}_{\mathrm{dec}}\Big(\hat{\tau}^{\hat{\tau}_i}_i(\tau) - \hat{\tau}^{\hat{\tau}_j}_j\big(\tau - d^{\hat{\tau}_i}_{\mathrm{dll}\,\leftarrow\,\mathrm{pbs}} \\ - R^{\hat{\tau}_i}_{ij}\big(\tau - d^{\hat{\tau}_i}_{\mathrm{dll}\,\leftarrow\,\mathrm{pbs}}\big) \\ - d^{\hat{\tau}_j}_{\mathrm{pbs}\,\leftarrow\,\mathrm{pmc}}\big)\Big) \\ = \mathbf{D}^{\mathrm{prn},\,\hat{\tau}_i}_{\mathrm{dec}\,\leftarrow\,\mathrm{pbs}}\, R^{\hat{\tau}_i}_{ij}(\tau) + O^{\mathrm{prn}}_{ij}. \qquad (21)\end{aligned}$$

The on-board delays cause a timestamping delay $\mathbf{D}^{\mathrm{prn}}_{\mathrm{dec}\,\leftarrow\,\mathrm{pbs}}$, the PRN timestamping delay, and an offset O^{prn}_{ij}, the PRNR offset:

$$\begin{aligned}\mathbf{D}^{\mathrm{prn}}_{\mathrm{dec}\,\leftarrow\,\mathrm{pbs}} = \mathbf{D}^{\mathrm{prn}}_{\mathrm{dec}}\,\mathbf{D}_{\mathrm{dll}}\,\mathbf{D}^{\mathrm{prn}}_{\mathrm{dpll}}\,\mathbf{D}_{\mathrm{dpll}\,\leftarrow\,\mathrm{abee}} \\ \mathbf{D}^{\mathrm{prn}}_{\mathrm{abee}}\,\mathbf{D}_{\mathrm{abee}\,\leftarrow\,\mathrm{qpr}}\,\mathbf{D}^{\mathrm{prn}}_{\mathrm{qpr}} \\ \mathbf{D}_{\mathrm{qpr}\,\leftarrow\,\mathrm{bs}}\,\mathbf{D}_{\mathrm{bs}\,\leftarrow\,\mathrm{pbs}}, \qquad (22)\end{aligned}$$

$$O^{\mathrm{prn}}_{ij} = d^{\hat{\tau}_i}_{\mathrm{dll}\,\leftarrow\,\mathrm{pbs}} + d^{\hat{\tau}_j}_{\mathrm{pbs}\,\leftarrow\,\mathrm{pmc}}. \qquad (23)$$

The PRN timestamping delay has similar constituents as the common carrier delay, they are marked pink in fig. 3. However, most of them are frequency or amplitude dependent. Therefore, they differ between carrier and PRN signals. As for the common carrier delay, we propose to individually calibrate all constituents of the PRN timestamping delay on ground before mission start. Hence, during operation $\mathbf{D}^{\mathrm{prn}}_{\mathrm{dec}\,\leftarrow\,\mathrm{pbs}}$ can be compensated in an initial data treatment by application of its associated advancement operator $\mathbf{A}^{\mathrm{prn}}_{\mathrm{pbs}\,\leftarrow\,\mathrm{dec}}$. After that, the PRNR observation equation including ranging noise and PRN ambiguity can be written as:

$$\begin{aligned}\mathbf{A}^{\mathrm{prn},\,\hat{\tau}_i}_{\mathrm{pbs}\,\leftarrow\,\mathrm{dec}}\,\mathrm{PRNR}^{\hat{\tau}_i}_{ij}(\tau) = R^{\hat{\tau}_i}_{ij}(\tau) + O^{\mathrm{prn}}_{ij} + N^{\mathrm{prn}}_{ij}(\tau) \\ - a^{\mathrm{prn}}_{ij}(\tau)\cdot l. \qquad (24)\end{aligned}$$

l denotes the finite PRN code length. We use 400 km as a placeholder, the final value has not been decided. The finite PRN code length leads to an ambiguity, a^{prn}_{ij} denote the associated ambiguity integers [8]. N^{prn}_{ij} is the white ranging noise with an RMS amplitude of about 1m at 4 Hz. This ranging noise is mainly due to shot noise and PRN code interference [9]. The PRNR offset O^{prn}_{ij} involves contributions on the emitter and on the receiver side (see eq. 23), they are marked light blue in fig. 3. It can amount to 10 m and more [17, 18]. Similar to the common carrier and the PRN timestamping delay, we propose to calibrate the PRNR offset on ground, so that it can be subtracted in an initial data treatment.

C. Sideband ranging (SBR)

For the purpose of in-band clock noise reduction in the INReP, a clock noise transfer between the SC is implemented [9]: the 80 MHz PMC signals are up-converted to $\nu^{\mathrm{m}}_l = 2.400\,\mathrm{GHz}$ and $\nu^{\mathrm{m}}_r = 2.401\,\mathrm{GHz}$ for left and right-handed MOSAs, respectively (see fig. 2 for the definition of left and right-handed MOSAs). The EOMs phase-modulate the carriers with the up-converted PMC signals, thereby creating clock sidebands.[3] We show below that the beatnotes between these clock sidebands constitute a pseudorange observable.

Considering on-board delays, the difference between carrier and sideband beatnotes can be written as

$$\begin{aligned}\mathrm{ISI}^{\hat{\tau}_i}_{ij}(\tau) - \mathrm{ISI}^{\hat{\tau}_i}_{\mathrm{sb},\,ij}(\tau) = -\,\mathbf{D}^{\mathrm{sb},\,\hat{\tau}_i}_{\mathrm{dec}\,\leftarrow\,\mathrm{bs}} \\ \Big\{\mathbf{D}^{\hat{\tau}_i}_{\mathrm{bs}\,\leftarrow\,\mathrm{pbs}}\,\mathbf{D}^{\hat{\tau}_i}_{ij}\Big(\mathbf{D}^{\mathrm{sb},\,\hat{\tau}_j}_{\mathrm{pbs}\,\leftarrow\,\mathrm{pmc}}\,\nu^{\mathrm{m}}_{ji}\,\hat{\tau}^{\hat{\tau}_j}_j(\tau) + \nu^{\mathrm{m}}_{ji}\,M^{\hat{\tau}_j}_{ji}(\tau)\Big) \\ -\Big(\mathbf{D}^{\mathrm{sb},\,\hat{\tau}_i}_{\mathrm{bs}\,\leftarrow\,\mathrm{pmc}}\,\nu^{\mathrm{m}}_{ij}\,\hat{\tau}^{\hat{\tau}_i}_i(\tau) + \nu^{\mathrm{m}}_{ij}\,M^{\hat{\tau}_i}_{ij}(\tau)\Big)\Big\}. \qquad (25)\end{aligned}$$

$\mathbf{D}^{\mathrm{sb}}_{\mathrm{pbs}\,\leftarrow\,\mathrm{pmc}}$ and $\mathbf{D}^{\mathrm{sb}}_{\mathrm{bs}\,\leftarrow\,\mathrm{pmc}}$ are the delay operators associated to the paths from the PMC to the PBS and to the ISI BS, respectively. They can be decomposed into:

$$\mathbf{D}^{\mathrm{sb}}_{(\mathrm{p})\mathrm{bs}\,\leftarrow\,\mathrm{pmc}} = \mathbf{D}_{(\mathrm{p})\mathrm{bs}\,\leftarrow\,\mathrm{eom}}\,\mathbf{D}_{\mathrm{eom}\,\leftarrow\,\mathrm{pmc}}\,\mathbf{D}_{\mathrm{up}}, \qquad (26)$$

$\mathbf{D}_{\mathrm{up}}$ is the up-conversion delay due to phase-locking a 2.40(1) GHz oscillator to the the 80 MHz PMC signal, $\mathbf{D}_{\mathrm{eom}\,\leftarrow\,\mathrm{pmc}}$ is the cable delay from the PMC to the EOM. ν^{m}_{ij} is the up-converted USO frequency associated to MOSA_{ij}. Since eq. 25 is expressed in the SCET, all clock imperfections are included in $\hat{\tau}^{\hat{\tau}_i}_i(\tau)$. The modulation noise $M^{\hat{\tau}_i}_{ij}$ contains any additional jitter collected on the path $\mathbf{D}^{\mathrm{sb}}_{(\mathrm{p})\mathrm{bs}\,\leftarrow\,\mathrm{pmc}}$, e.g., due to the electrical frequency up-converters. The amplitude spectral densities (ASDs) of the modulation noise for left and right-handed MOSAs are specified to be below [6, 19]

$$\sqrt{S_{M_l}(f)} = 2.5\times10^{-6}\,\mathrm{m\,Hz^{-0.5}}\left(\frac{f}{\mathrm{Hz}}\right)^{-2/3}, \qquad (27)$$

$$\sqrt{S_{M_r}(f)} = 2.5\times10^{-5}\,\mathrm{m\,Hz^{-0.5}}\left(\frac{f}{\mathrm{Hz}}\right)^{-2/3}. \qquad (28)$$

The modulation noise on left-handed MOSAs is one order of magnitude lower, because the pilot tone used for the ADC jitter correction, hence being the ultimate phase reference, is derived from the 2.400 GHz clock signal.

To derive a pseudorange observation equation from the sideband beatnote we expand eq. 25 using eq. 2. We apply the advancement operator $\mathbf{A}^{\mathrm{sb}}_{\mathrm{pbs}\,\leftarrow\,\mathrm{dec}}$ to avoid nested delays in the pseudorange:

$$\begin{aligned}\mathbf{A}^{\mathrm{sb},\,\hat{\tau}_i}_{\mathrm{pbs}\,\leftarrow\,\mathrm{dec}}\Big(\mathrm{ISI}^{\hat{\tau}_i}_{ij}(\tau) - \mathrm{ISI}^{\hat{\tau}_i}_{\mathrm{sb},\,ij}(\tau)\Big) \\ = \nu^{\mathrm{m}}_{ij}\,\mathbf{A}^{\hat{\tau}_i}_{\mathrm{pbs}\,\leftarrow\,\mathrm{bs}}\Big(\mathbf{D}^{\mathrm{sb},\,\hat{\tau}_i}_{\mathrm{bs}\,\leftarrow\,\mathrm{pmc}}\,\hat{\tau}^{\hat{\tau}_i}_i(\tau) + M^{\hat{\tau}_i}_{ij}\Big) \\ - \nu^{\mathrm{m}}_{ji}\,\mathbf{D}^{\hat{\tau}_i}_{ij}\Big(\mathbf{D}^{\mathrm{sb},\,\hat{\tau}_j}_{\mathrm{pbs}\,\leftarrow\,\mathrm{pmc}}\,\hat{\tau}^{\hat{\tau}_j}_j(\tau) + M^{\hat{\tau}_j}_{ji}(\tau)\Big) \\ = \left(\nu^{\mathrm{m}}_{ij} - \nu^{\mathrm{m}}_{ji}\right)\tau + \nu^{\mathrm{m}}_{ji}\,R^{\hat{\tau}_i}_{ij}(\tau) \\ + \nu^{\mathrm{m}}_{ji}\cdot d^{\hat{\tau}_j}_{\mathrm{pbs}\,\leftarrow\,\mathrm{pmc}} - \nu^{\mathrm{m}}_{ij}\cdot\Big(d^{\hat{\tau}_i}_{\mathrm{bs}\,\leftarrow\,\mathrm{pmc}} - d^{\hat{\tau}_i}_{\mathrm{pbs}\,\leftarrow\,\mathrm{bs}}\Big) \\ + \nu^{\mathrm{m}}_{ij}\,\mathbf{A}^{\hat{\tau}_i}_{\mathrm{pbs}\,\leftarrow\,\mathrm{bs}}\,M^{\hat{\tau}_i}_{ij}(\tau) - \nu^{\mathrm{m}}_{ji}\,\mathbf{D}^{\hat{\tau}_i}_{ij}M^{\hat{\tau}_j}_{ji}(\tau). \qquad (29)\end{aligned}$$

[3] We focus on the first order upper clock sidebands, because the lower sidebands contain almost the same information.

We subtract the 1 MHz ramp and then refer to eq. 29 as sideband ranging (SBR). Taking into account that the SBR phase is defined up to a cycle, the SBR can be written as

$$\begin{aligned}\mathrm{SBR}_{ij}^{\hat{\tau}_i}(\tau) &= \mathbf{A}^{\mathrm{sb},\,\hat{\tau}_i}_{\mathrm{pbs}\,\leftarrow\,\mathrm{dec}}\left(\mathrm{ISI}_{ij}^{\hat{\tau}_i}(\tau) - \mathrm{ISI}^{\hat{\tau}_i}_{\mathrm{sb},\,ij}(\tau)\right) \pm 1\,\mathrm{MHz}\,\tau \\ &= \nu^{\mathrm{m}}_{ji}\, R_{ij}^{\hat{\tau}_i}(\tau) + O^{\mathrm{sb}}_{ij} + N^{\mathrm{sb}}_{ij}(\tau) - a^{\mathrm{sb}}_{ij}(\tau). \end{aligned} \tag{30}$$

a^{sb}_{ij} denote the SBR ambiguity integers. Expressed as length, the SBR ambiguity is 12.5 cm corresponding to the wavelength of the GHz sidebands. The SBR offset

$$\begin{aligned}O^{\mathrm{sb}}_{ij} &= \nu^{\mathrm{m}}_{ji}\cdot d^{\hat{\tau}_j}_{\mathrm{pbs}\,\leftarrow\,\mathrm{pmc}} \\ &\quad - \nu^{\mathrm{m}}_{ij}\cdot\left(d^{\hat{\tau}_i}_{\mathrm{bs}\,\leftarrow\,\mathrm{pmc}} - d^{\hat{\tau}_i}_{\mathrm{pbs}\,\leftarrow\,\mathrm{bs}}\right)\end{aligned} \tag{31}$$

can be thought of as the differential phase accumulation of local and distant PMC signals on their paths to the respective PBSs. Similar to the PRNR offset and the various delays, the SBR offset should be measured on ground. N^{sb}_{ij} denotes the appearance of the modulation noise in the SBR:

$$N^{\mathrm{sb}}_{ij}(\tau) = \nu^{\mathrm{m}}_{ij}\,\mathbf{A}^{\hat{\tau}_i}_{\mathrm{pbs}\,\leftarrow\,\mathrm{bs}}\,M^{\hat{\tau}_i}_{ij}(\tau) - \nu^{\mathrm{m}}_{ji}\,\mathbf{D}^{\hat{\tau}_i}_{ij}M^{\hat{\tau}_j}_{ji}(\tau). \tag{32}$$

This is a combination of left and right-handed modulation noise, their RMS amplitudes are 2.9×10^{-5} m and 2.9×10^{-4} m, respectively. As shown in [6], it is possible to combine carrier and sideband beatnotes from the RFI to form measurements of the dominating right-handed modulation noise, which can, thus, be subtracted from the SBRs (see appendix B).

The advancement operator $\mathbf{A}^{\mathrm{sb}}_{\mathrm{pbs}\,\leftarrow\,\mathrm{dec}}$ (see eq. 29) is associated to the delay operator $\mathbf{D}^{\mathrm{sb}}_{\mathrm{dec}\,\leftarrow\,\mathrm{pbs}}$, to which we refer as sideband timestamping delay. The sideband timestamping delay can be decomposed into:

$$\begin{aligned}\mathbf{D}^{\mathrm{sb}}_{\mathrm{dec}\,\leftarrow\,\mathrm{pbs}} &= \mathbf{D}^{\mathrm{sb}}_{\mathrm{dec}}\,\mathbf{D}^{\mathrm{sb}}_{\mathrm{dpll}}\,\mathbf{D}_{\mathrm{dpll}\,\leftarrow\,\mathrm{abee}}\,\mathbf{D}^{\mathrm{sb}}_{\mathrm{abee}} \\ &\quad \mathbf{D}_{\mathrm{abee}\,\leftarrow\,\mathrm{qpr}}\,\mathbf{D}^{\mathrm{sb}}_{\mathrm{qpr}}\,\mathbf{D}_{\mathrm{qpr}\,\leftarrow\,\mathrm{bs}},\end{aligned} \tag{33}$$

these constituents are marked dark yellow in fig. 3. As for the common carrier and the PRN timestamping delay, we propose to individually calibrate all its constituents on ground. The sideband timestamping delay can then be compensated in an initial data treatment by application of its associated advancement operator (see eq. 29).

In reality, the beatnotes are expected to be delivered not in phase, but in frequency with occasional phase anchor points. Therefore, we consider the derivative of eq. 30, we refer to it as sideband range rate (SBR):

$$\dot{\mathrm{SBR}}_{ij}^{\hat{\tau}_i}(\tau) = \nu^{\mathrm{m}}_{ji}\,\dot{R}^{\hat{\tau}_i}_{ij}(\tau) + \dot{N}^{\mathrm{sb}}_{ij}(\tau). \tag{34}$$

The sideband range rates are an offset-free and unambiguous measurement of the pseudorange time derivatives. Phase anchor points enable their integration, so that we recover eq. 30.

D. Time-delay interferometric ranging (TDIR)

TDI builds combinations of delayed ISI and RFI carrier beatnotes to virtually form equal-arm interferometers, in which laser frequency noise is suppressed. In the alternative TDI topology, the corresponding delays are given by the pseudoranges in combination with the small optical path lengths between laser, PBS, and ISI BS (see the uncommon carrier delay eq. 12). Time delay interferometric ranging (TDIR) turns this approach upside-down: it minimizes the power integral of the laser frequency noise in the TDI combinations by varying the delays that are applied to the beatnotes [12]. When doing this before clock synchronization to TCB, i.e., with the beatnotes sampled according to the respective SCETs, the uncommon delays show up at the very minimum of that integral. Thus, TDIR constitutes a pseudorange observable.

Below, we consider TDI in frequency [14]. We introduce the Doppler-delay operator, which can be considered as the time derivative of the interspacecraft delay operator (see eq. 4):

$$\dot{\mathbf{D}}^{\hat{\tau}_i}_{ij}\,f^{\hat{\tau}_j}(\tau) = \left(1-\dot{R}^{\hat{\tau}_i}_{ij}(\tau)\right)\cdot f^{\hat{\tau}_j}\left(\tau - R^{\hat{\tau}_i}_{ij}(\tau)\right). \tag{35}$$

We use the shorthand notation

$$\dot{\mathbf{D}}^{\hat{\tau}_i}_{ijk} = \dot{\mathbf{D}}^{\hat{\tau}_i}_{ij}\,\dot{\mathbf{D}}^{\hat{\tau}_j}_{jk} \tag{36}$$

to indicate chained interspacecraft Doppler-delay operators. In this paper we neglect on-board delays in the RFI beatnotes. We start our consideration of TDIR from the intermediary TDI variables η_{ij}. These are combinations of the ISI and RFI carrier beatnotes to eliminate the laser frequency noise contributions of right-handed lasers. In terms of the η_{ij} the second-generation TDI Michelson variables can be expressed as [20]

$$\begin{aligned}X_2^{\hat{\tau}_1} &= \left(1-\dot{\mathbf{D}}^{\hat{\tau}_1}_{121}-\dot{\mathbf{D}}^{\hat{\tau}_1}_{12131}+\dot{\mathbf{D}}^{\hat{\tau}_1}_{1312121}\right)\left(\eta^{\hat{\tau}_1}_{13}-\dot{\mathbf{D}}^{\hat{\tau}_1}_{13}\eta^{\hat{\tau}_3}_{31}\right) \\ &- \left(1-\dot{\mathbf{D}}^{\hat{\tau}_1}_{131}-\dot{\mathbf{D}}^{\hat{\tau}_1}_{13121}+\dot{\mathbf{D}}^{\hat{\tau}_1}_{1213131}\right)\left(\eta^{\hat{\tau}_1}_{12}-\dot{\mathbf{D}}^{\hat{\tau}_1}_{12}\eta^{\hat{\tau}_2}_{21}\right)\end{aligned} \tag{37}$$

$Y_2^{\hat{\tau}_2}(\tau)$ and $Z_2^{\hat{\tau}_3}(\tau)$ are obtained by cyclic permutation of the indices. For later reference, we also state the first generation TDI Michelson variables:

$$\begin{aligned}X_1^{\hat{\tau}_1} &= \left(1-\dot{\mathbf{D}}^{\hat{\tau}_1}_{121}\right)\left(\eta^{\hat{\tau}_1}_{13}-\dot{\mathbf{D}}^{\hat{\tau}_1}_{13}\eta^{\hat{\tau}_3}_{31}\right) \\ &- \left(1-\dot{\mathbf{D}}^{\hat{\tau}_1}_{131}\right)\left(\eta^{\hat{\tau}_1}_{12}-\dot{\mathbf{D}}^{\hat{\tau}_1}_{12}\eta^{\hat{\tau}_2}_{21}\right).\end{aligned} \tag{38}$$

In the framework of TDIR, the delays applied in TDI are parameterized by a model, e.g., by a polynomial model. We minimize the power integral of the TDI combinations by varying the model parameters. TDIR attempts to minimize the in-band laser frequency noise residual. Therefore, we apply a band-pass filter to first remove other contributions appearing out-of-band, i.e.,

slow drifts and contributions above 1Hz that are dominated by aliasing and interpolation errors. The TDIR pseudorange observables for the second generation TDI Michelson variables can then be expressed as

$$\mathrm{TDIR}_{ij}^{\hat{\tau}_i} = \min_{\Theta} \frac{1}{T} \int_{\frac{1}{T}}^{T} \left[\tilde{X}_2^{\hat{\tau}_1}\right]^2 + \left[\tilde{Y}_2^{\hat{\tau}_2}\right]^2 + \left[\tilde{Z}_2^{\hat{\tau}_3}\right]^2 \mathrm{d}t, \tag{39}$$

Θ denotes the parameters of the delay model, the tilde indicates the filtered TDI combinations.

The TDIR accuracy, we denote it by σ^{tdir}, increases with the integration time T (length of telemetry dataset). It is in the order of [12]:

$$\sigma^{\mathrm{tdir}}(T) \propto 10\,\mathrm{cm}\,\sqrt{\frac{\mathrm{d}}{T}}, \tag{40}$$

where d stands for day.

E. Ground-observation based ranging (GOR)

The mission operation center (MOC) provides orbit determinations (ODs) via the ESA tracking stations and MOC time correlations (MOC-TCs). When combined properly, these two on-ground measurements form a pseudorange observable referred to as ground-observation based ranging (GOR). It has an uncertainty of about 50 km due to uncertainties in both the OD and the MOC-TC. Yet, it yields valuable information. It is unambiguous, hence it allows to resolve the PRNR ambiguities.

The OD yields information about the absolute positions and velocities of the three SC. New orbit determinations are published every few days. For the position and velocity measurements in the line of sight, radial (with respect to the sun) and cross-track direction conservative estimations by ESA state the uncertainties as 2 km and $4\,\mathrm{mm\,s^{-1}}$, 10 km and $4\,\mathrm{mm\,s^{-1}}$, 50 km and $5\,\mathrm{cm\,s^{-1}}$, respectively [21]. The MOC-TC is a measurement of the SCET desynchronization from TCB. It is determined during the telemetry contacts via a comparison of the SCET associated to the emission of a telemetry packet and the TCB of its reception on Earth taking into account the down link delay. We expect the accuracy of the MOC-TC to be better than 0.1 ms (corresponds to 30 km). This uncertainty is due to unexact knowledge of the SC-to-ground-station separation, as well as inaccuracies in the time tagging process on board and on ground.

As shown in appendix A, the pseudoranges can be expressed in TCB as functions of the reception time:

$$R_{ij}^t(t) = (1 + \delta\dot{\hat{\tau}}_j^t(t)) \cdot d_{ij}^t(t) + \delta\hat{\tau}_{ij}^t(t). \tag{41}$$

d_{ij}^t denotes the light travel time from SC j to SC i, $\delta\hat{\tau}_{ij}^t$ the offset between the involved SCETs, and $\delta\dot{\hat{\tau}}_j^t$ the SCET drift of the emitting SC with respect to TCB. The light travel times can be expressed in terms of the ODs [22]:

$$d_{\mathrm{od},\,ij}^t(t) = \frac{1}{c} L_{ij}^t(t) + \frac{1}{c^2}\,\vec{L}_{ij}^t(t) \cdot \vec{v}_j^t(t) + O(c^{-3}), \tag{42}$$

$$\vec{L}_{ij} = \vec{r}_i - \vec{r}_j,\; L_{ij} = |\vec{L}_{ij}|, \tag{43}$$

$\vec{r}_i$ denoting the position of the receiving SC, $\vec{r}_j$ and $\vec{v}_j$ the position and the velocity of the emitting one, respectively. The terms of order $O(c^{-3})$ contribute to the light travel time at the order of 10 m and are therefore negligible compared to the large uncertainties of the orbit determination. Combining the light travel times obtained this way with the MOC-TC allows to write the GOR as

$$\mathrm{GOR}_{ij}^t(t) = d_{\mathrm{od},\,ij}^t(t) + \delta\hat{\tau}_{\mathrm{tc},\,i}^t(t) - \delta\hat{\tau}_{\mathrm{tc},\,j}^t(t) + N_{ij}^{\mathrm{gor}}(t). \tag{44}$$

$\delta\hat{\tau}_{\mathrm{tc},\,i}^t$ denotes the MOC-TC of SC i and $N_{\mathrm{gor}}^t \sim 50\,\mathrm{km}$ the GOR uncertainty. Note that OD and MOC-TC, and hence also the GOR, are given in TCB, while all other pseudorange observables are sampled in the respective SCETs. This desynchronization is negligible: the desynchronization can amount up to 10 s after the ten year mission time, the pseudoranges drift with 10 to $100\,\mathrm{m\,s^{-1}}$ (see central plot in fig. 5). Hence, neglecting the desynchronization leads to an error in the order of 100 to 1000 m, which is negligible compared to the large GOR uncertainty.

III. RANGING SENSOR FUSION

To combine the four pseudorange observables, we propose a three-stage ranging sensor fusion consisting of an initial data treatment, a ranging processing, and crosschecks. The ranging processing (central part of fig. 4) refers to the ranging-related routines, which need to run continuously during operation. These are the PRNR unwrapping, and the reduction of ranging and right-handed modulation noise. Simultaneously, the PRNR ambiguities and offsets are steadily crosschecked using TDIR and GOR (lower part of fig. 4). Both ranging processing and crosschecks rely on a preceding initial data treatment (upper part of fig. 4), in which the various delays and offsets are compensated for. Ranging processing and crosschecks can be categorized into four parts demonstrated below: PRNR ambiguity, noise, PRNR offset, and SBR ambiguity.

A. PRNR ambiguity

As part of the ranging processing, the PRNR needs to be steadily unwrapped: due to the finite PRN code length, the PRNR jumps back to 0 km when crossing 400 km and vice versa (see upper plot in fig. 5). These jumps are unphysical but easy to track and to remove.

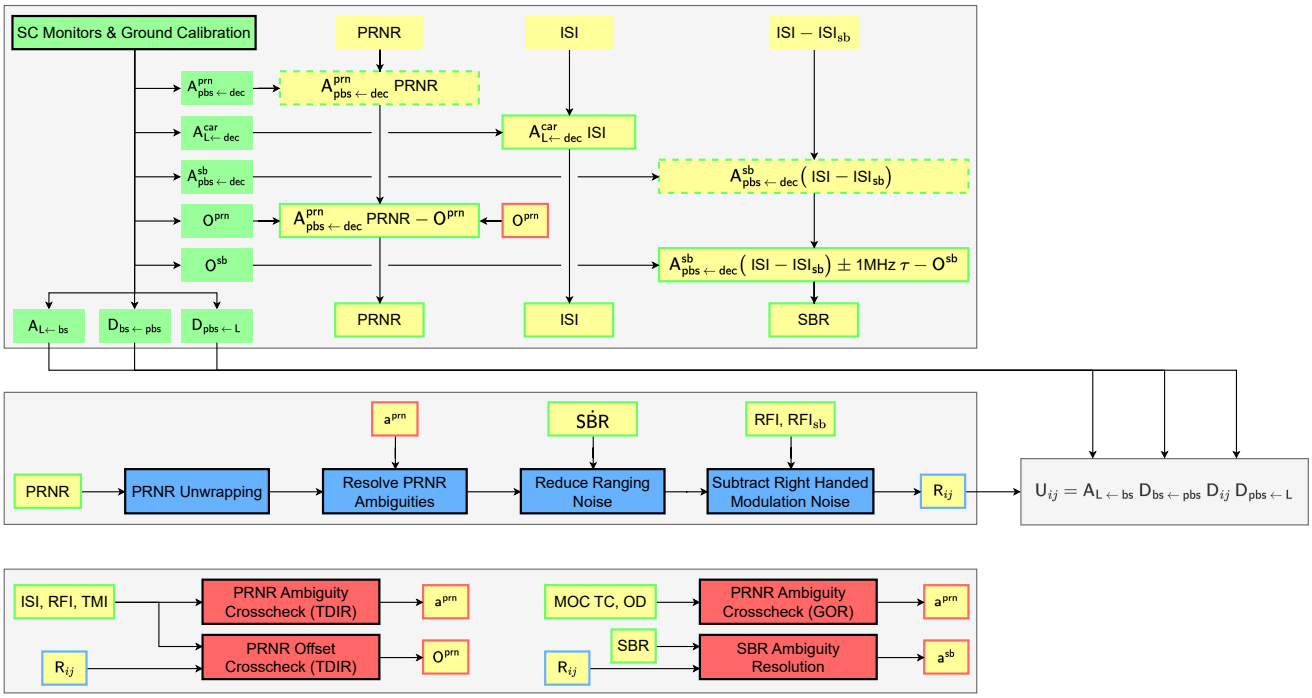

Figure 4. We illustrate the three-stage ranging sensor fusion. Processing elements are drawn with a black frame. In the upper part we show the initial data treatment. Products of the on-ground calibration (the various delays and offsets) are drawn green. Raw datasets are drawn yellow, after the initial data treatment we add a green frame. In the central part we show the core ranging processing. Its output, the pseudoranges, are drawn with a blue frame. In the right box we show how the pseudoranges are combined with the small optical path length to form the uncommon delays (the delays for TDI). In the lower part we show simultaneous crosschecks of PRNR ambiguity, PRNR offset, and SBR ambiguity. Products of these crosschecks are drawn with a red frame. We do not consider the on-board delays of the RFI and TMI beatnotes.

Apart from that, the PRNR ambiguities need to be crosschecked regularly. For that purpose we propose two independent methods below.

The combination of PRNR and GOR enables an identification of the PRNR ambiguity integers a_{ij}^{prn}:

$$\mathrm{GOR}_{ij}^{t}(t) - \mathrm{PRNR}_{ij}^{\hat{\tau}_i}(\tau) = N_{ij}^{\mathrm{gor}} + a_{ij}^{\mathrm{prn}}(\tau)\cdot 400\,\mathrm{km} + \underbrace{R_{ij}^{t}(t) - R_{ij}^{\hat{\tau}_i}(\tau) - O_{ij}^{\mathrm{prn}} - N_{ij}^{\mathrm{prn}}(\tau)}_{\text{negligible}}, \quad (45)$$

$$a_{ij}^{\mathrm{prn}}(\tau) = \mathrm{round}\left[\frac{\mathrm{GOR}_{ij}^{t}(t) - \mathrm{PRNR}_{ij}^{\hat{\tau}_i}(\tau)}{400\,\mathrm{km}}\right], \quad (46)$$

400 km is the value we assumed for the PRN code length. However, this procedure only succeeds if $|N_{ij}^{\mathrm{gor}}|$ does not exceed the PRN code's half length, i.e., 200 km. Otherwise, a wrong value for the associated PRN ambiguity integer is selected resulting in an estimation error of 400 km in the corresponding link. Note that $\mathrm{GOR}_{ij}^{t}(t)$ and $\mathrm{PRNR}_{ij}^{\hat{\tau}_i}(\tau)$ are sampled according to different time frames, but this desynchronization is negligible considering the low accuracy that needs to be reached here (see section II E).

TDIR constitutes an unambiguous pseudorange observable too. It can be applied as an independent crosscheck of the PRNR ambiguities. We linearly detrend the ISI, RFI, and TMI beatnotes. We then form the first-generation TDI Michelson variables (see eq. 38) assuming constant delays. It is not necessary to apply second-generation TDI, the first-generation already accomplishes the task (see fig. 8). The pseudoranges are actually drifting by 10 to 100 $\mathrm{m\,s^{-1}}$ mainly due to differential USO frequency offsets (see central plot in fig. 5). Therefore, we choose a short integration time (we use 150 s), otherwise the constant delay model is not sufficient. We use the GOR for the initial delay values of the TDIR estimator. The TDIR pseudorange estimates can then be used to crosscheck the PRNR ambiguity integers:

$$a_{ij}^{\mathrm{prn}}(\tau) = \mathrm{round}\left[\frac{\mathrm{TDIR}_{ij}^{\hat{\tau}_i}(\tau) - \mathrm{PRNR}_{ij}^{\hat{\tau}_i}(\tau)}{400\,\mathrm{km}}\right]. \quad (47)$$

B. Noise reduction

For the ranging noise reduction in the ranging processing, we propose to combine PRNR and sideband range rates in a linear Kalman filter (KF). The conventional KF requires all measurements to be sampled according to one overall time grid. However, in LISA each SC involves

its own SCET. We circumvent this difficulty by splitting up the system and build one KF per SC. Each KF only processes the measurements taken on its associated SC, so that the individual SCETs serve as time-grids.

The state vector of the KF belonging to SC 1 and its associated linear system model can be expressed as

$$x^{\hat{\tau}_1} = (R_{12}^{\hat{\tau}_1},\, R_{13}^{\hat{\tau}_1},\, \dot{R}_{12}^{\hat{\tau}_1},\, \dot{R}_{13}^{\hat{\tau}_1},\, \ddot{R}_{12}^{\hat{\tau}_1},\, \ddot{R}_{13}^{\hat{\tau}_1})^\intercal, \tag{48}$$

$$x_{k+1}^{\hat{\tau}_1} = \begin{pmatrix} 1 & 0 & \Delta t & 0 & \frac{\Delta t^2}{2} & 0 \\ 0 & 1 & 0 & \Delta t & 0 & \frac{\Delta t^2}{2} \\ 0 & 0 & 1 & 0 & \Delta t & 0 \\ 0 & 0 & 0 & 1 & 0 & \Delta t \\ 0 & 0 & 0 & 0 & 1 & 0 \\ 0 & 0 & 0 & 0 & 0 & 1 \end{pmatrix} \cdot x_k^{\hat{\tau}_1} + w_k^{\hat{\tau}_1}, \tag{49}$$

k being a discrete time index. Eq. 49 describes the time evolution of the state vector from k to $k+1$. $w_k^{\hat{\tau}_1}$ denotes the process noise vector, its covariance matrix is given by

$$\mathrm{E}\left[w_k \cdot w_l^{\mathrm{T}}\right] = \delta_{k,\,l}\, W, \tag{50}$$

$$W = \mathrm{diag}\Big(\, 0,\, 0,\, 0,\, 0,\, 10^{-15}\mathrm{s}^{-1},\, 10^{-15}\mathrm{s}^{-1}\Big)^2. \tag{51}$$

$\delta_{k,\,l}$ denotes the Kronecker delta. Hence, eq. 50 indicates that each component of $w_k^{\hat{\tau}_1}$ is a white random process. The process noise covariance matrix we used in our implementation is given in eq. 51. The measurement vector and the associated observation model are given by

$$y^{\hat{\tau}_1} = (\mathrm{PRNR}_{12}^{\hat{\tau}_1},\, \mathrm{PRNR}_{13}^{\hat{\tau}_1},\, \mathrm{S\dot{B}R}_{12}^{\hat{\tau}_1},\, \mathrm{S\dot{B}R}_{13}^{\hat{\tau}_1})^\intercal, \tag{52}$$

$$y_k^{\hat{\tau}_1} = \begin{pmatrix} 1 & 0 & 0 & 0 & 0 & 0 \\ 0 & 1 & 0 & 0 & 0 & 0 \\ 0 & 0 & 2.401\,\mathrm{GHz} & 0 & 0 & 0 \\ 0 & 0 & 0 & 2.400\,\mathrm{GHz} & 0 & 0 \end{pmatrix} \cdot x_k^{\hat{\tau}_1} + v_k^{\hat{\tau}_1}. \tag{53}$$

Eq. 53 relates the measurement vector to the state vector. $v_k^{\hat{\tau}_1}$ denotes the measurement noise vector, its covariance matrix is given by

$$\mathrm{E}\left[v_k \cdot v_l^{\mathrm{T}}\right] = \delta_{k,\,l}\, V, \tag{54}$$

$$V = \mathrm{diag}\Big(\, 3\cdot 10^{-9}\mathrm{m\,s}^{-1},\, 3\cdot 10^{-9}\mathrm{m\,s}^{-1},\, 5.2\cdot 10^{-13},\, 5.2\cdot 10^{-13}\Big)^2. \tag{55}$$

The measurement noise covariance matrix we used in our implementation is given in eq. 55. The diagonal entries denote the variances of the respective measurements. We assume the measurements to be uncorrelated, so that the off-diagonal terms are zero. The KFs for SC 2 and SC 3 are defined accordingly. In this manner, we remove the ranging noise and obtain estimates for the six pseudoranges and their time derivatives.

These pseudorange estimates are dominated by the right-handed modulation noise, which is one order of magnitude higher than the left-handed one. As pointed out in [6], the right-handed modulation noise can be subtracted (see appendix B): we combine the RFI measurements to form the ΔM_i, which are measurements of the right-handed modulation noise on SC i (see eq. B4). For right-handed MOSAs, the local right-handed modulation noise enters the sideband range rates and we just need to subtract the local ΔM_i (see eq. B5b). For left-handed MOSAs the Doppler-delayed right-handed modulation noise from the distant SC appears in the sideband range rates. Here we need to apply the Kalman filter estimates for the pseudoranges and their time derivatives to form the Doppler-delayed distant ΔM_i, which then can be subtracted (see eq. B5a). We then process the three KFs again, this time with the corrected sideband range rates. Nowe they are limited by left-handed modulation noise, so that the respective noise levels are lower. Therefore, we need to adjust the measurement noise covariance matrix for the second run of the KFs:

$$V_{\mathrm{cor}} = \mathrm{diag}\Big(3\cdot 10^{-9}\mathrm{m\,s}^{-1},\, 3\cdot 10^{-9}\mathrm{m\,s}^{-1},\, 7.4\cdot 10^{-14},\, 7.4\cdot 10^{-14}\Big)^2. \tag{56}$$

In this way we obtain estimates for the pseudoranges and their time derivatives, which are limited by the left-handed modulation noise.

C. PRNR offset

The PRNR offset is calibrated on ground before mission start. During operation, it is constructed with the help of SC monitors and subtracted in the initial data treatment.

TDIR can be used as a crosscheck for residual PRNR offsets, as it is sensitive to offsets in the delays. To obtain optimal performance we choose the second-generation TDI Michelson variables to be ultimately limited by secondary noises. In-band clock noise is sufficiently suppressed, since we operate on beatnotes in total frequency and make use of the in-band ranging information provided by the preceding noise reduction step. Accordingly, the offset delay model is parameterized by

$$d_{ij}^{\hat{\tau}_i}(\tau) = \hat{R}_{ij}^{\hat{\tau}_i}(\tau) - O_{ij}, \tag{57}$$

$\hat{R}_{ij}^{\hat{\tau}_i}$ denote the pseudorange estimates after noise reduction, O_{ij} are the 6 offset parameters. As discussed in section II D, computing TDI in total frequency units generally results in a variable with residual trends. Those trends need to be removed prior to calculation of the TDIR integral to be sensitive to residual laser noise in band. This is achieved by an appropriate band-pass filter with a pass-band from 0.1 Hz to 1 Hz. The TDIR integral then reads

$$\hat{O}_{ij} = \underset{O_{ij}}{\arg\min} \int_0^T \tilde{X}^2(t) + \tilde{Y}^2(t) + \tilde{Z}^2(t)\,\mathrm{d}t \tag{58}$$

where tilde indicates the filtered quantity.

D. SBR ambiguity

Phase anchor points, together with the pseudorange estimates after noise reduction, enable the resolution of the SBR ambiguity (see eq. 30):

$$a_{ij}^{\mathrm{sb}}(\tau) = \mathrm{round}\left[\nu_{ji}^{\mathrm{m}}\,\hat{R}_{ij}^{\hat{\tau}_i}(\tau) - \mathrm{SBR}_{ij}^{\hat{\tau}_i}(\tau)\right]. \tag{59}$$

$\mathrm{SBR}_{ij}^{\hat{\tau}_i}$ are the phase anchor points, $\hat{R}_{ij}^{\hat{\tau}_i}$ the pseudorange estimates after noise reduction. Thus, we obtain estimates of the SBR ambiguity integers a_{ij}^{sb}. The resolution is successful if the pseudorange estimates are more accurate than 6.25 cm (half the ambiguity). From the perspective of noise reduction, this is feasible (see section IV). Having resolved the SBR ambiguity, the pseudorange estimates associated to the phase anchor points serve as initial values for the integration of the sideband range rates. The resolution of the SBR ambiguity is worthwhile: SBR constitutes a very accurate pseudorange observable, as both its stability and accuracy are limited by the modulation noise.

IV. RESULTS

In this section, we demonstrate the performance of our implementation of the core ranging processing and the crosschecks as proposed in section III (central and lower part of fig. 4). We did not implement the initial data treatment. Instead we assume that the common carrier, PRN, and sideband timestamping delays are compensated beforehand. We further consider offset-free PRNR and apply TDIR as a crosscheck for residual offsets.

We use telemetry data simulated by LISA Instrument [23] and LISANode [24] based on orbits provided by ESA [21, 25]. We simulate phase anchor points for the SBR (see eq. 30). The SCET deviations from the respective proper times are modeled by

$$\delta\hat{\tau}_i(\tau) = \delta\hat{\tau}_{i,\,0} + y_i\,\tau + \frac{\dot{y}_i}{2}\,\tau^2 + \frac{\ddot{y}_i}{3}\,\tau^3 + \int_{\tau_0}^{\tau} \mathrm{d}\tilde{\tau}\; y_i^{\epsilon}(\tilde{\tau}), \tag{60}$$

the $\delta\hat{\tau}_{i,\,0}$ denote the initial SCET deviations set to 1 s, −1.2 s, and 0.6 s for SC 1, 2, and 3, respectively. The y_i model the PMC frequency offsets corresponding to linear clock drifts. They are set to 10^{-7}, -2×10^{-7}, and 0.6×10^{-7} for SC 1, 2, and 3, respectively. $\dot{y}_i \sim 10^{-14}\,\mathrm{s}^{-1}$ and $\ddot{y}_i \sim 10^{-23}\,\mathrm{s}^{-2}$ are constants modeling the linear and quadratic PMC frequency drifts. The y_i^{ϵ} denote the stochastic clock noise in fractional frequency deviations, the associated ASD is given by

$$\sqrt{S_{y^{\epsilon}}(f)} = 6.32\times10^{-14}\mathrm{Hz}^{-0.5}\left(\frac{f}{\mathrm{Hz}}\right)^{-0.5}. \tag{61}$$

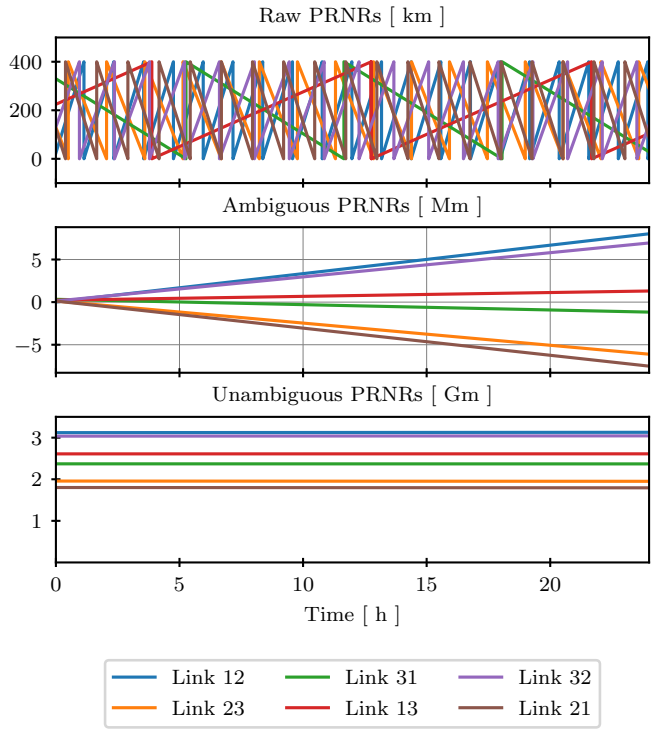

Figure 5. Upper plot: raw PRNR. The ambiguity jumps at 0 km and 400 km can be seen. Central plot: ambiguous PRNR, the jumps have been removed but the PRNR ambiguities have not been resolved yet. The large slopes are mainly due to USO frequency offsets. Lower plot: unambiguous PRNR. The large differences between the links are caused by differential SCET offsets.

We simulate laser frequency noise with an ASD of

$$\sqrt{S_{\dot{N}^{\mathrm{p}}}(f)} = 30\,\mathrm{Hz}\,\mathrm{Hz}^{-0.5}, \tag{62}$$

and ranging and modulation noise as specified in the sections II B and II C. Furthermore, we consider test-mass acceleration noise

$$\sqrt{S_{N^{\delta}}(f)} = 4.8\times10^{-15}\mathrm{m\,s^{-2}\,Hz^{-0.5}}\sqrt{1+\left(\frac{0.4\,\mathrm{mHz}}{f}\right)^2} \tag{63}$$

and readout noise

$$\sqrt{S_{N^{\mathrm{ro}}}(f)} = A\sqrt{1+\left(\frac{2\,\mathrm{mHz}}{f}\right)^4}, \tag{64}$$

where $A = 6.35\times10^{-12}\mathrm{m\,Hz^{-0.5}}$ for the ISI carrier and $A = 1.25\times10^{-11}\mathrm{m\,Hz^{-0.5}}$ for the ISI sideband beatnotes. For the readout noise we set a saturation frequency of $f_{\mathrm{sat}} = 0.1\,\mathrm{mHz}$, below which we whiten. The orbit determinations are simulated by LISA Ground Tracking with the noise levels specified in section II.

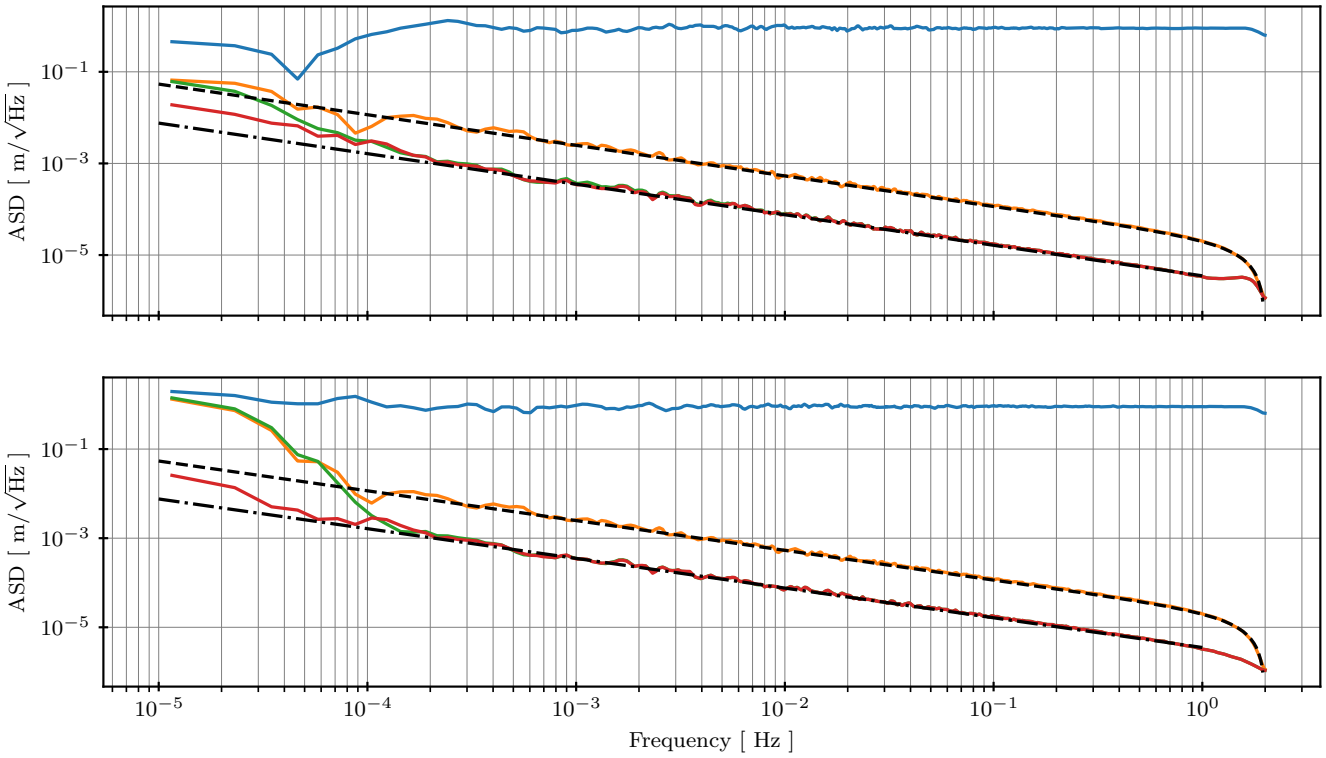

Figure 6. ASDs of the residual pseudorange estimates for link 12 (upper plot) and link 21 (lower plot). In blue, residual PRNR. In orange, residual pseudorange estimates after ranging noise reduction. In green, residual pseudorange estimates after subtraction of right-handed modulation noise. In red, residual SBR. Dashed black lines, right-handed modulation noise model. Dash-dotted black lines, left-handed modulation noise model.

A. Ranging processing

Here we demonstrate the performance of our implementation of the core ranging processing for one day of telemetry data simulated by LISA Instrument [23]. The first ranging processing step covers the PRNR unwrapping (see fig. 5). The upper plot shows the raw PRNR, which jumps back to 0 km when crossing 400 km and vice versa. These jumps are easy to track and to remove. In our implementation we remove all PRNR jumps bigger than 200 km. The central plot shows the unwrapped but yet ambiguous PRNR. Here you can see PRNR drifts of the order of 10 to 100 $\mathrm{m\,s^{-1}}$, which are mainly due to differential USO frequency offsets. Inserting the PRNR ambiguity integers obtained from GOR and TDIR yields the unambiguous PRNR shown in the lower plot.

In the second step, we use the Kalman filter presented in section III to reduce the ranging noise. Subsequently, we subtract the right-handed modulation noise applying the ΔM measurements constructed from the RFI beatnotes (see appendix B). After noise reduction, we resolve the SBR ambiguities combining the estimated pseudoranges with the simulated SBR phase anchor points (see eq. 59). We then integrate the sideband range rates, to obtain unambiguous SBR.

In fig. 6, we plot the ASDs of the residual pseudorange estimates (deviations of the estimates from the true pseudorange values in the simulation) for link 12 (upper plot) and link 21 (lower plot). Blue lines show the ASDs of the residual PRNR, which are essentially the ASDs of the white ranging noises. The residual pseudorange estimates after ranging noise reduction are plotted in orange. They are obtained by combining the PRNR with the sideband range rates. Therefore, they are limited by right-handed modulation noise (dashed black line). In green, we plot the residual pseudorange estimates after subtraction of right-handed modulation noise with the RFI beatnotes. Now the estimates are limited by left-handed modulation noise (dash-dotted black line). The residual SBR are drawn red, they are limited by left-handed modulation noise as well, but involve a smaller offset, since the SBR phase anchor points are more accurate than PRNR after ranging noise reduction (see fig. 7). In the case of left-handed MOSAs (see link 12) the RFI beatnotes need to be time shifted to form the delayed ΔM measurements. We apply the time shifting method of PyTDI [26], which consists in a Lagrange interpolation (we use order 5). The interpolation introduces noise in the high frequency band (see the bump at 2 Hz in the upper plot) but this is out of band.

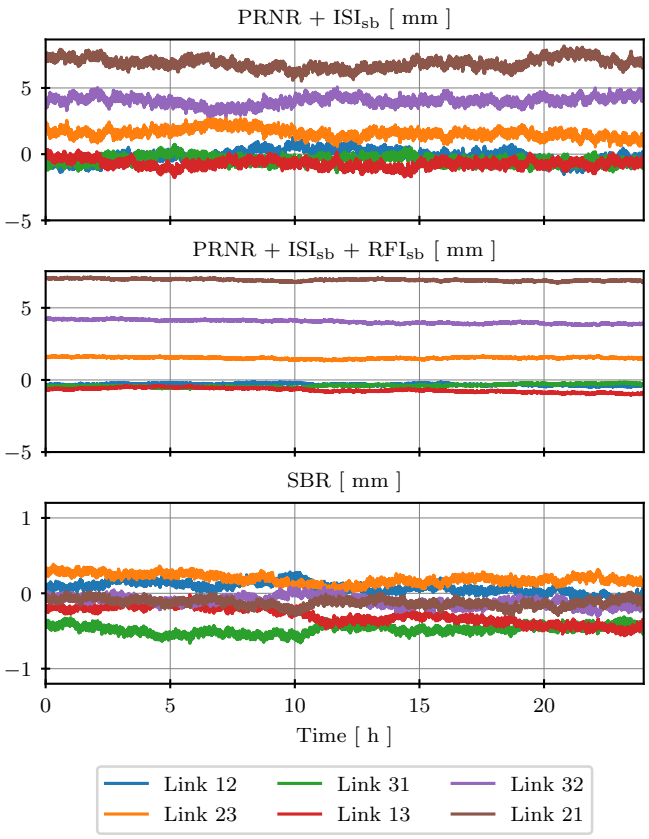

Figure 7. Upper plot: residual pseudorange estimates after ranging noise reduction. Second plot: residual pseudorange estimates after subtraction of right-handed modulation noise. Third plot: residual SBR estimates.

Fig. 7 shows the different residual pseudorange estimates as time series. The upper plot shows the 6 residual pseudorange estimates after ranging noise reduction, the second plot after subtraction of right-handed modulation noise. The third plot shows the SBR residuals. The subtraction of right-handed modulation noise reduces the noise floor, but it does not increase the accuracy of the pseudorange estimates. The accuracy can be increased by one order of magnitude through the resolution of the SBR ambiguities. After ambiguity resolution, SBR constitutes pseudorange estimates with sub-mm accuracy.

B. Crosschecks

Here we demonstrate the performance of our implementation of the crosschecks for PRNR ambiguity and PRNR offset.

The PRNR ambiguities can be resolved using either GOR (see eq. 46) or TDIR (see eq. 47). To evaluate the performance of both methods, we simulate 1000 short (150 s) telemetry datasets with LISA Instrument [23], and one set of ODs and MOC-TCs for each of them. We compute the GOR and TDIR pseudorange estimates for each of the 1000 datasets. Fig. 8 shows the GOR residuals (first row) and the TDIR residuals (second row) in km as histogram plots. We see that the GOR accuracy depends on the arm, because we obtain more accurate ODs for arms oriented in line of sight direction than for those oriented cross-track. The PRNR ambiguity resolution via GOR is successful for GOR deviations smaller than 200 km. In the case of the links 23, 31, 13, and 32 all PRNR ambiguity resolutions via GOR are successful. For each of the links 12 and 21, 2 out of the 1000 PRNR ambiguity resolutions fail. The GOR estimates are passed as initial values to TDIR, which then reduces the uncertainty by almost one order of magnitude (lower plot of fig. 8), such that eventually all PRNR ambiguity resolutions are successful.

TDIR can also be applied to estimate the PRNR offsets. Hence, it constitutes a cross-check of the on-ground PRNR offset calibration. We simulate one year of telemetry data using LISANode [24]. We set the PRNR offsets to 160.3 m, −210.2 m, 137.3 m, −250.3 m, −188.8 m, and 105.1 m for the links 12, 23, 31, 13, 32, and 21, respectively. We divide the dataset into 1 day chunks (left plots in fig. 9), 2 day chunks (central plots in fig. 9), and 3 day chunks (right plots in fig. 9). In each partition we apply the TDIR estimator presented in section III C to each chunk in order to estimate the PRNR offsets. This computation was parallelized and executed on the ATLAS cluster at the AEI Hannover. In the upper part of fig. 9 we show the offset estimation residuals for the three chunk sizes. The offset estimation accuracy increases with the chunk size in agreement with the order of magnitude estimate through eq. 40. In the lower part of fig. 9 we plot the residual cumulative averages of the PRNR offset estimates for the different chunk sizes. Here, it can be seen that the TDIR estimator performs similarly for the different chunk sizes. With the 3 day chunk size we can estimate all PRNR offsets with an accuracy of better than 20 cm after 10 days. The dashed-black lines indicate 6.25 cm (half the SBR ambiguity). This is the required PRNR offset estimation accuracy for a successful SBR ambiguity resolution. With the 3 day chunk size all offset estimation residuals are below these 6.25 cm after 179 days.

V. CONCLUSION

The reduction of laser frequency noise in TDI crucially depends on information about the pseudoranges. There are four pseudorange observables each having advantages and disadvantages. In this article, we first derived their observation equations carefully taking into account ambiguities, noise, and on-board delays, which cause offsets and timestamping delays. We then proposed a three-stage ranging sensor fusion (initial data treatment, ranging processing, crosschecks, compare fig. 4) to combine

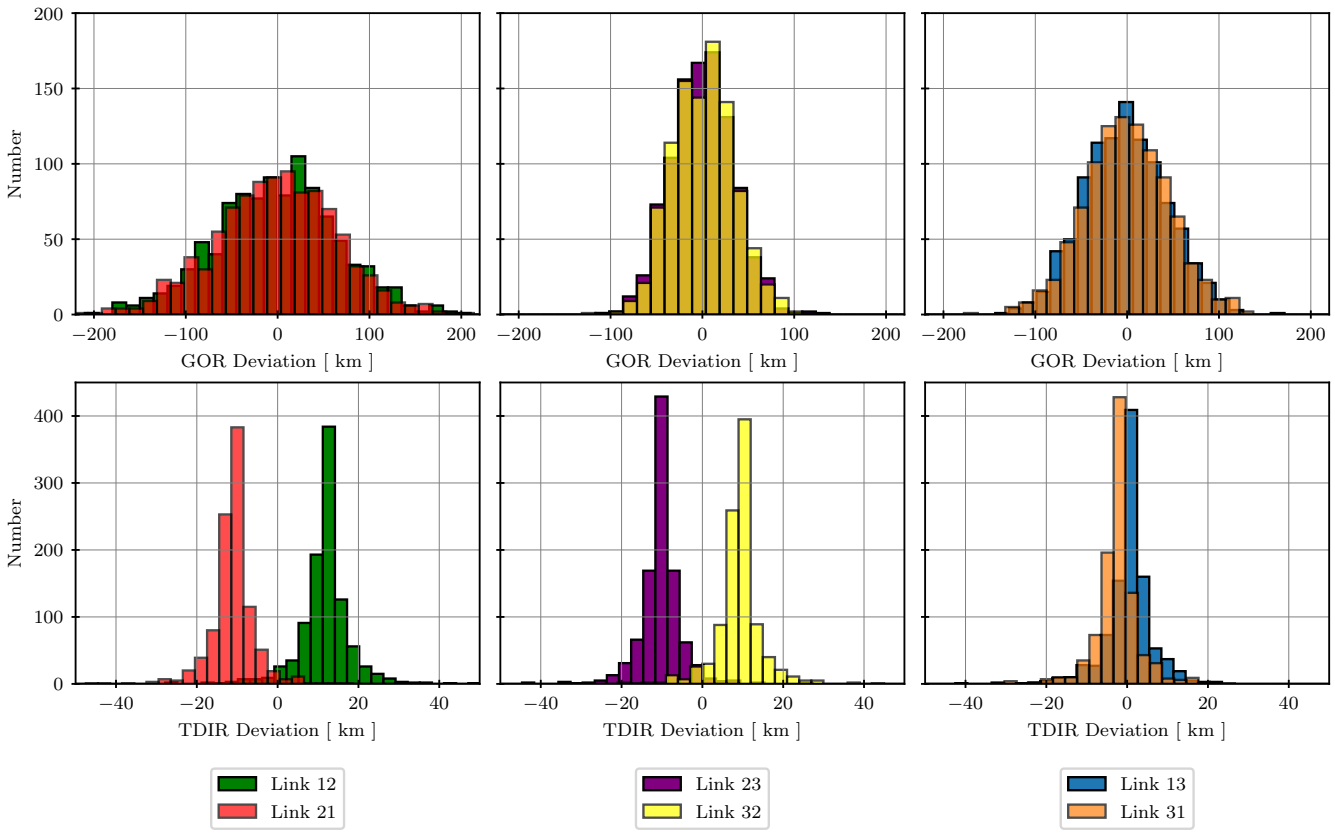

Figure 8. PRNR ambiguity resolution via GOR (upper plots) and TDIR (lower plots). The histogram plots show the residual GOR and TDIR pseudorange estimates for the different links.

the four pseudorange observables, such that we obtain optimal pseudorange estimates.

We pointed out that the common carrier, PRN, and sideband timestamping delays (see eqs. 16, 22, and 33), as well as the PRNR and SBR offsets (see eqs. 23 and 26) need to be calibrated on ground, so that they can be compensated in the initial data treatment. We further derived that the small optical path lengths between laser and PBS, PBS and ISI BS, and laser and ISI BS show up in the uncommon delays (see eq. 12), which are to be applied in TDI. We proposed to measure these optical path lengths on ground, so that during operation they can be combined with the pseudorange estimates to form the uncommon delays.

We identified the processing steps, which need to be performed continuously during operation. These are the PRNR unwrapping, and the reduction of ranging and right-handed modulation noise, we referred to them as ranging processing. We implemented the ranging processing numerically: we showed that the white ranging noise can be reduced by combining the PRNR with the sideband range rates in a KF. We split up the system and implemented one KF per SC, such that the individual SCETs served as KF time-grids. We further applied the RFI beatnotes to subtract the right-handed modulation noise. The pseudorange estimates we obtained this way were at sub-cm accuracy. We showed that in combination with phase anchor points they allow for the resolution of the SBR ambiguity resulting in pseudorange estimates at sub-mm accuracy.

We implemented crosschecks for the PRNR ambiguities and offsets. We showed that both GOR and TDIR allow for the resolution of the PRNR ambiguity. We applied TDIR as a crosscheck for the PRNR offset calibration and demonstrated its performance for one year of telemetry data: after about 180 days all PRNR offset estimates reached an accuracy of better than 6.25 cm allowing for the resolution of the SBR ambiguity.

In reality, the PRNR offsets are slowly time-varying. The investigation of the PRNR offset estimation via TDIR could be extended for linearly time varying PRNR offsets. The delay model for the TDIR estimator would then become (compare eq. 57):

$$d_{ij}^{\hat{\tau}_i}(\tau) = \hat{R}_{ij}^{\hat{\tau}_i}(\tau) - (O_{ij}^0 + O_{ij}^1 \cdot \tau), \tag{65}$$

The TDIR estimator would now have to fit the 12 parameters O_{ij}^0 and O_{ij}^1. Apart from that, tone-assisted TDIR [27] could be applied for the PRNR offset esti-

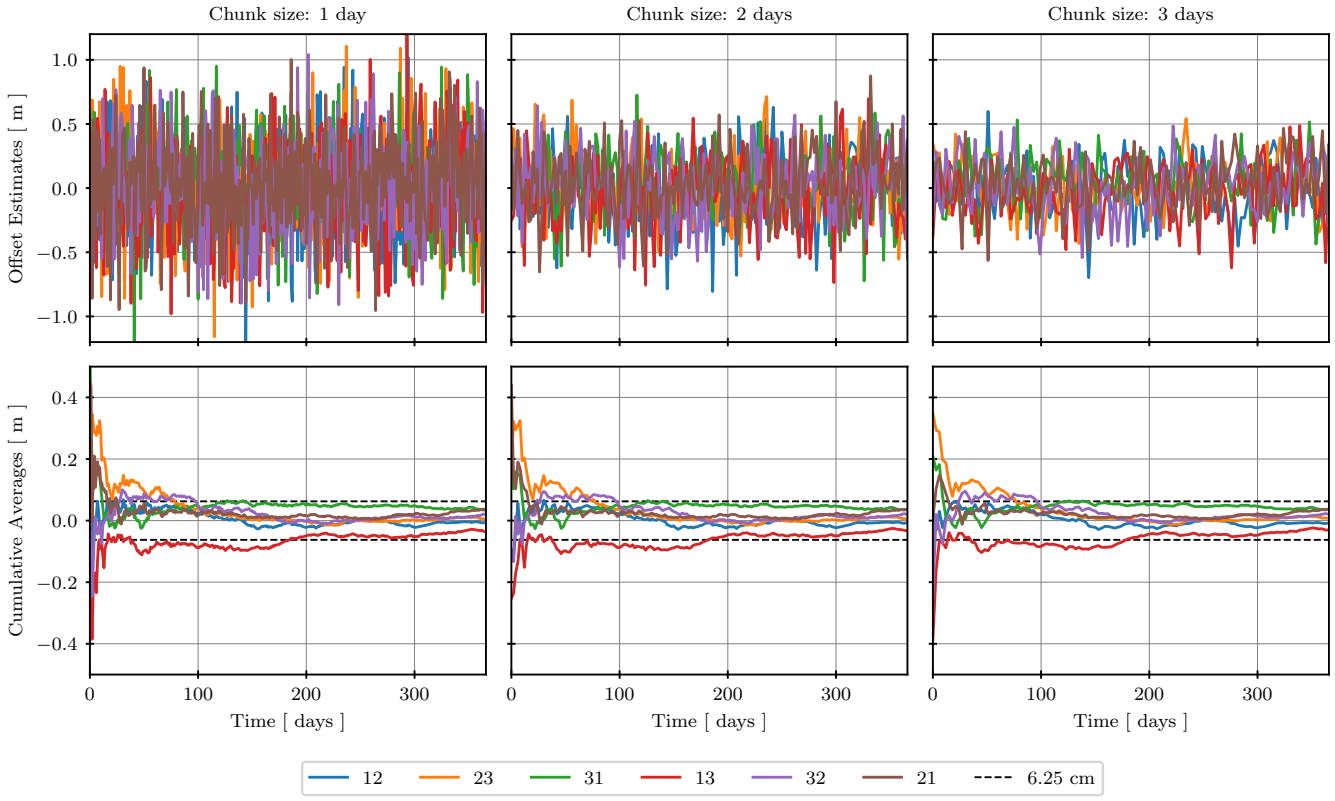

Figure 9. We simulate one year of telemetry data with PRNR offsets in the order of 100 m. We divide this dataset into 1 day chunks (left plots), 2 day chunks (central plots), and 3 day chunks (right plots). We then we apply TDIR to each of these chunks in order to estimate the PRNR offsets. Upper plots: Residual offset estimates in m for the different chunk sizes. Lower plots: residual offset estimates after cumulative averaging in m for the different chunk sizes. Dashed-black lines: half the SBR ambiguity.

mation in order to reach faster convergence. As a further follow-up investigation, time-varying on-board delays and the associated SC monitors could be included into the simulation, which would enable an inspection of the feasibility of the initial data treatment as proposed in section III. Furthermore, the ranging sensor fusion could be included into the different INReP topologies. Apart from that, the algorithms could be applied to real data as, e.g., produced by the hexagon experiment [28], [29].

ACKNOWLEDGEMENTS

J. N. R. acknowledges the funding by the Deutsche Forschungsgemeinschaft (DFG, German Research Foundation) under Germany's Excellence Strategy within the Cluster of Excellence PhoenixD (EXC 2122, Project ID 390833453). Furthermore, he acknowledges the support by the IMPRS on Gravitational Wave-Astronomy at the Max Planck Institute for Gravitational Physics in Hannover, Germany. This work is also supported by the Max-Planck-Society within the LEGACY ("Low-Frequency Gravitational-Wave Astronomy in Space") collaboration (M.IF.A.QOP18098). O. H. and A. H. acknowledge support from the Programme National GRAM of CNRS/INSU with INP and IN2P3 co-funded by CNES and from the Centre National d'Études Spatiales (CNES). The authors thank Miles Clark, Pascal Grafe, Waldemar Martens, and Peter Wolf for useful discussions. The study on PRNR offset estimation via TDIR was performed on the ATLAS cluster at AEI Hannover. The authors thank Carsten Aulbert and Henning Fehrmann for their support.

Appendix A: Pseudoranges in TCB

The pseudorange can be expressed in TCB by writing the SCETs of receiving and emitting SC as functions of TCB evaluated at the events of reception and emission, respectively:

$$R^t_{ij}(t_{\rm rec}) = \hat{\tau}^t_i(t_{\rm rec}) - \hat{\tau}^t_j(t_{\rm emit}), \tag{A1}$$

$\hat{\tau}^t_i$ denotes the SCET of SC i expressed as a function of TCB. The TCB of emission can be expressed as the

difference between the TCB of reception and the light travel time from SC j to SC i, denoted by d^t_{ij}:

$$R^t_{ij}(t_{\rm rec}) = \hat{\tau}^t_i(t_{\rm rec}) - \hat{\tau}^t_j\left(t_{\rm rec} - d^t_{ij}(t_{\rm rec})\right), \tag{A2}$$

in the following we drop the subscript, hence t refers to the TCB of reception. The SCET can be expressed in terms of the SCET deviation from TCB

$$\hat{\tau}^t_i(t) = t + \delta\hat{\tau}^t_i(t), \tag{A3}$$

which allows us to write eq. A2 as

$$R^t_{ij}(t) = \delta\hat{\tau}^t_i(t) + d^t_{ij}(t) + \delta\hat{\tau}^t_j(t - d^t_{ij}(t). \tag{A4}$$

Expanding the emitting SC SCET deviation from TCB around the reception TCB yields:

$$R^t_{ij}(t) = \delta\hat{\tau}^t_{ij}(t) + \left(1 + \delta\dot{\hat{\tau}}^t_j(t)\right)\cdot d^t_{ij}(t), \tag{A5}$$

$$\delta\hat{\tau}^t_{ij}(t) := \delta\hat{\tau}^t_i(t) - \delta\hat{\tau}^t_j(t). \tag{A6}$$

Hence, in a global time frame like TCB, the pseudorange can be expressed in terms of the light travel time d^t_{ij} and the differential SCET offset $\delta\hat{\tau}^t_{ij}$.

Appendix B: Subtraction of right-handed modulation noise

Following the notation in [6], we express the RFI beatnotes in frequency:

$$\mathrm{RFI}^{\hat{\tau}_i}_{ij}(\tau) = \nu^{\hat{\tau}_i}_{ik}(\tau) - \nu^{\hat{\tau}_i}_{ij}(\tau), \tag{B1}$$

$$\mathrm{RFI}^{\hat{\tau}_i}_{\mathrm{sb},\,ij}(\tau) = \nu^{\hat{\tau}_i}_{\mathrm{sb},\,ik}(\tau) - \nu^{\hat{\tau}_i}_{\mathrm{sb},\,ij}(\tau), \tag{B2}$$

$$\nu^{\hat{\tau}_i}_{\mathrm{sb},\,ij}(\tau) = \nu^{\hat{\tau}_i}_{ij}(\tau) + \nu^{\mathrm{m}}_{ij}\cdot(1 + M^{\hat{\tau}_i}_{ij}). \tag{B3}$$

In this article we do not consider on-board delays in the RFI beatnotes. We combine the RFI carrier and sideband beatnotes to form measurements of the right-handed modulation noise:

$$\begin{aligned}\Delta M^{\hat{\tau}_i}_i :=& \frac{\mathrm{RFI}^{\hat{\tau}_i}_{ij} - \mathrm{RFI}^{\hat{\tau}_i}_{\mathrm{sb},\,ij} + 1\,\mathrm{MHz}}{2}\\ &- \frac{\mathrm{RFI}^{\hat{\tau}_i}_{ik} - \mathrm{RFI}^{\hat{\tau}_i}_{\mathrm{sb},\,ik} - 1\,\mathrm{MHz}}{2},\\ =& \nu^{\mathrm{m}}_{ij}\cdot M^{\hat{\tau}_i}_{ij} - \nu^{\mathrm{m}}_{ik}\cdot M^{\hat{\tau}_i}_{ik},\end{aligned} \tag{B4}$$

i, j, and k being a cyclic permutation of 1, 2, and 3. We can now subtract the $\Delta M^{\hat{\tau}_i}_i$ measurements from the sideband range rates (eq. 34). Thus, we reduce the right-handed modulation noise, so that we are limited by the one order of magnitude lower left-handed modulation noise:

$$\begin{aligned}\dot{\mathrm{SBR}}^{\hat{\tau}_i}_{\mathrm{cor},\,ij} =& \dot{\mathrm{SBR}}^{\hat{\tau}_i}_{ij} - \dot{\mathbf{D}}^{\hat{\tau}_i}_{ij}\cdot\Delta M^{\hat{\tau}_j}_j(\tau),\\ =& \nu^{\mathrm{m}}_{ji}\cdot\dot{R}^{\hat{\tau}_i}_{ij} + \nu^{\mathrm{m}}_{ij}\left(M^{\hat{\tau}_i}_{ij} - \dot{\mathbf{D}}^{\hat{\tau}_i}_{ij}\cdot M^{\hat{\tau}_j}_{jk}(\tau)\right),\end{aligned} \tag{B5a}$$

$$\begin{aligned}\dot{\mathrm{SBR}}^{\hat{\tau}_i}_{\mathrm{cor},\,ik} =& \dot{\mathrm{SBR}}^{\hat{\tau}_i}_{ik}(\tau) + \Delta M^{\hat{\tau}_i}_i(\tau),\\ =& \nu^{\mathrm{m}}_{ki}\cdot\dot{R}^{\hat{\tau}_i}_{ik} + \nu^{\mathrm{m}}_{ki}\left(M^{\hat{\tau}_i}_{ij} + \dot{\mathbf{D}}^{\hat{\tau}_i}_{ik}\,M^{\hat{\tau}_k}_{ki}(\tau)\right),\end{aligned} \tag{B5b}$$

i, j, and k being a cyclic permutation of 1, 2, and 3.

Appendix C: Solar wind dispersion

The average solar wind particle density at the LISA orbit is about $10\,\mathrm{cm}^{-3}$. Hence, at the scales of optical wavelengths the solar wind plasma can be treated as a free electron gas with the plasma frequency [30]

$$\nu_p^2 = \frac{n_e\,e^2}{4\pi^2\,\epsilon_0\,m_e} \approx 8\times10^8\,\mathrm{s}^{-2}, \tag{C1}$$

n_e denotes the electron density, e the elementary charge, m_e the electron mass, and ϵ_0 the the vacuum permittivity. Contributions from protons and ions can be neglected as the plasma frequency is inversely proportional to the mass. We describe the refractive index of the solar wind plasma by the Appleton equation. Neglecting collisions and magnetic fields it denotes

$$n(\nu) = \sqrt{1 - \left(\frac{\nu_p}{\nu}\right)^2}. \tag{C2}$$

In a dispersive medium we need to distinguish between phase and group velocity. The phase velocity is given by

$$v_{\rm p}(\nu) = \frac{c}{n(\nu)} = \frac{c}{\sqrt{1-\left(\frac{\nu_p}{\nu}\right)^2}} \approx c\cdot\left(1 + \frac{1}{2}\frac{\nu_p^2}{\nu^2}\right), \tag{C3}$$

where we applied the expansion for $\nu \gg \nu_p$, as we consider optical frequencies. The product of group and phase velocity yields c^2. Consequently, the group velocity is

$$v_{\rm g}(\nu) = c\cdot n(\nu) = c\cdot\sqrt{1-\left(\frac{\nu_p}{\nu}\right)^2} \approx c\cdot\left(1 - \frac{1}{2}\frac{\nu_p^2}{\nu^2}\right). \tag{C4}$$

Group and phase delay can now be written as

$$\Delta\tau_{\rm g}(\nu) = L\left(\frac{1}{c\cdot\sqrt{1-\left(\frac{\nu_p}{\nu}\right)^2}} - \frac{1}{c}\right) \approx \frac{L\,\nu_p^2}{2\,c}\cdot\frac{1}{\nu^2}, \tag{C5}$$

$$\Delta\tau_{\rm p}(\nu) = L\left(\frac{\sqrt{1-\left(\frac{\nu_p}{\nu}\right)^2}}{c} - \frac{1}{c}\right) \approx -\frac{L\,\nu_p^2}{2\,c}\cdot\frac{1}{\nu^2}, \tag{C6}$$

where $L = 2.5\,\mathrm{Gm}$ denotes the LISA armlength. PRN and sideband signals propagate at the group velocity, hence they are delayed by the group delay:

$$\Delta\tau_{\rm g}^{\rm prn} = \Delta\tau_{\rm g}(281\,\mathrm{THz} \pm 1\,\mathrm{MHz}) \approx 12.7\,\mathrm{pm}, \tag{C7}$$

$$\Delta\tau_{\rm g}^{\rm sb} = \Delta\tau_{\rm g}(281\,\mathrm{THz} \pm 2.4\,\mathrm{GHz}) \approx 12.7\,\mathrm{pm}. \tag{C8}$$

The phase delay is negative, because the phase velocity is bigger than c. Therefore, the laser phase is advanced with respect to a wave propagating in vacuum. For the LISA carrier this phase advancement corresponds to

$$\Delta\tau_{\rm p}(281\,\mathrm{THz}) \approx -12.7\,\mathrm{pm}. \tag{C9}$$

[1] P. Amaro-Seoane, H. Audley, S. Babak, J. Baker, E. Barausse, P. Bender, E. Berti, P. Binetruy, M. Born, D. Bortoluzzi, *et al.*, Laser interferometer space antenna, arXiv preprint arXiv:1702.00786 (2017).

[2] O. Gerberding, B. Sheard, I. Bykov, J. Kullmann, J. J. E. Delgado, K. Danzmann, and G. Heinzel, Phasemeter core for intersatellite laser heterodyne interferometry: modelling, simulations and experiments, Classical and Quantum Gravity **30**, 235029 (2013).

[3] S. Barke, N. Brause, I. Bykov, J. J. Esteban Delgado, A. Enggaard, O. Gerberding, G. Heinzel, J. Kullmann, S. M. Pedersen, and T. Rasmussen, LISA metrology system-final report, (2014).

[4] J. Armstrong, F. Estabrook, and M. Tinto, Time-delay interferometry for space-based gravitational wave searches, The Astrophysical Journal **527**, 814 (1999).

[5] M. Tinto, F. B. Estabrook, and J. Armstrong, Time-delay interferometry for LISA, Physical Review D **65**, 082003 (2002).

[6] O. Hartwig, J.-B. Bayle, M. Staab, A. Hees, M. Lilley, and P. Wolf, Time-delay interferometry without clock synchronization, Phys. Rev. D **105**, 122008 (2022).

[7] J. J. Esteban, I. Bykov, A. F. G. Marín, G. Heinzel, and K. Danzmann, Optical ranging and data transfer development for LISA, in *Journal of Physics: Conference Series*, Vol. 154 (IOP Publishing, 2009) p. 012025.

[8] J. J. Esteban, A. F. García, J. Eichholz, A. M. Peinado, I. Bykov, G. Heinzel, and K. Danzmann, Ranging and phase measurement for LISA, in *Journal of Physics: Conference Series*, Vol. 228 (IOP Publishing, 2010) p. 012045.

[9] G. Heinzel, J. J. Esteban, S. Barke, M. Otto, Y. Wang, A. F. Garcia, and K. Danzmann, Auxiliary functions of the LISA laser link: ranging, clock noise transfer and data communication, Classical and Quantum Gravity **28**, 094008 (2011).

[10] O. Hartwig, Instrumental modelling and noise reduction algorithms for the laser interferometer space antenna, (2021).

[11] Y. Wang, G. Heinzel, and K. Danzmann, First stage of LISA data processing: Clock synchronization and arm-length determination via a hybrid-extended Kalman filter, Physical Review D **90**, 064016 (2014).

[12] M. Tinto, M. Vallisneri, and J. Armstrong, Time-delay interferometric ranging for space-borne gravitational-wave detectors, Physical Review D **71**, 041101 (2005).

[13] J.-B. Bayle and O. Hartwig, Unified model for the LISA measurements and instrument simulations, Physical Review D **107**, 083019 (2023).

[14] J.-B. Bayle, O. Hartwig, and M. Staab, Adapting time-delay interferometry for LISA data in frequency, Physical Review D **104**, 023006 (2021).

[15] W. Brzozowski, D. Robertson, E. Fitzsimons, H. Ward, J. Keogh, A. Taylor, M. Milanova, M. Perreur-Lloyd, Z. Ali, A. Earle, *et al.*, The LISA optical bench: an overview and engineering challenges, Space Telescopes and Instrumentation 2022: Optical, Infrared, and Millimeter Wave **12180**, 211 (2022).

[16] G. F. Barranco and G. Heinzel, A DC-coupled, HBT-based transimpedance amplifier for the LISA quadrant photoreceivers, IEEE Transactions on Aerospace and Electronic Systems **57**, 2899 (2021).

[17] A. Sutton, K. McKenzie, B. Ware, and D. A. Shaddock, Laser ranging and communications for LISA, Optics Express **18**, 20759 (2010).

[18] P. Euringer, G. Hechenblaikner, F. Soualle, and W. Fichter, Performance analysis of sequential carrier- and code-tracking receivers in the context of high-precision space-borne metrology systems, arXiv preprint arXiv:2302.13819 (2023).

[19] S. Barke, *Inter-spacecraft frequency distribution for future gravitational wave observatories* (Hannover: Gottfried Wilhelm Leibniz Universität Hannover, 2015).

[20] M. Otto, Time-delay interferometry simulations for the laser interferometer space antenna, (2015).

[21] W. Martens and E. Joffre, Trajectory design for the ESA LISA mission, The Journal of the Astronautical Sciences **68**, 402 (2021).

[22] A. Hees, S. Bertone, and C. Le Poncin-Lafitte, Relativistic formulation of coordinate light time, doppler, and astrometric observables up to the second post-Minkowskian order, Physical Review D **89**, 064045 (2014).

[23] J.-B. Bayle, O. Hartwig, and M. Staab, LISA Instrument (2022).

[24] J.-B. Bayle, O. Hartwig, A. Petiteau, and M. Lilley, LISANode (2022).

[25] J.-B. Bayle, A. Hees, M. Lilley, C. Le Poncin-Lafitte, W. Martens, and E. Joffre, LISA Orbits (2022).

[26] M. Staab, J.-B. Bayle, and O. Hartwig, PyTDI (2023).

[27] S. P. Francis, D. A. Shaddock, A. J. Sutton, G. De Vine, B. Ware, R. E. Spero, W. M. Klipstein, and K. McKenzie, Tone-assisted time delay interferometry on GRACE Follow-On, Physical Review D **92**, 012005 (2015).

[28] K. Yamamoto, C. Vorndamme, O. Hartwig, M. Staab, T. S. Schwarze, and G. Heinzel, Experimental verification of intersatellite clock synchronization at LISA performance levels, Physical Review D **105**, 042009 (2022).

[29] T. S. Schwarze, G. F. Barranco, D. Penkert, M. Kaufer, O. Gerberding, and G. Heinzel, Picometer-stable hexagonal optical bench to verify LISA phase extraction linearity and precision, Physical review letters **122**, 081104 (2019).

[30] A. Smetana, Background for gravitational wave signal at LISA from refractive index of solar wind plasma, Monthly Notices of the Royal Astronomical Society: Letters **499**, L77 (2020).